# Numerical simulation of non-isothermal viscoelastic fluid flows using a VMS stabilized Finite Element formulation

Laura Moreno[1], Ramon Codina[1,2] and Joan Baiges[1]

[1]Universitat Politècnica de Catalunya, Jordi Girona 1-3, Edifici C1, 08034, Barcelona, Spain

[2]Centre Internacional de Mètodes Numèrics en Enginyeria, Gran Capità S/N, 08034 Barcelona, Spain

**Abstract**

The effect of temperature in viscoelastic fluid flows is studied applying a stabilized finite element formulation based on both a standard and a log-conformation reformulation (LCR), and the Variational Multiscale (VMS) method as stabilization technique. The log-conformation reformulation turns out to be crucial to solve the cases with a high Weissenberg number. Regarding temperature coupling, a two-way coupling strategy is employed: on the one hand, the dependence of viscoelastic fluid parameters on temperature is established, together with the addition of a new term to the energy equation which takes into account the stress work. The formulations and the iterative algorithms are validated in the well-known flow past a cylinder benchmark. Besides, the extension 1:3 case is studied, in which several scenarios are explored varying the values of the main dimensionless numbers that characterize the problem to see how the flow pattern and temperature distribution change along the channel.

Keywords: non-isothermal fluid flow, viscoelasticity, log-conformation reformulation, thermal coupling, variational sub-grid scales

## 1 Introduction

The production process of polymers is mostly non-isothermal in nature. Flow properties are strongly dependent both on rheology and temperature, therefore there is a high interest to understand and make predictions of such type of flows. The combination of high viscosities of polymeric melts and high deformation rates results in the transformation of large amounts of mechanical energy into heat, and consequently in a rising of the material temperature. This phenomenon is used in extruders where viscous dissipation is employed to enhance the melting of the materials. Melt polymer flows in the industry are characterized by very low Reynolds numbers and high Prandtl numbers, thus leading to fast hydrodynamic flow development but rather slow thermal development. As remarked in [1], the non-isothermal nonlinear flow is also particularly relevant in many applications, since it is the basis of many complex flow problems with viscoelastic and multiphase fluids. Airflow inside a combustion engine, polymer flow in injection molding, or fluid flow in heat exchange problems, are only a few examples of viscous fluids where the temperature is an important unknown.

Concerning viscoelastic materials, stresses now play an important role on the temperature and temperature history and not only on the deformation (and deformation history). Consequently, the temperature should be an independent variable in the constitutive equations for the stress tensor, as Peters & Baaijens [2] explain in their work. Moreover, the temperature dependence of the linear viscoelastic properties (such as the relaxation time $\lambda$) is described by the principle of *time-temperature superposition*. This principle states that all characteristic times of the material depend on temperature similarly and therefore this relation can be described through a function of the temperature. In literature, we have

found two main models [3]: the Williams-Landel-Ferry (WLF) function [4] which is widely employed or the Arrhenius relationship [5] (see [6] for a discussion between these two methods). Also, the *time-temperature superposition* principle holds for rheological properties at different constant temperatures, however, it does not describe the consequences of temperature changes in time and space. As it is explained in [2], another difficulty for solving non-isothermal viscoelastic flows comes from the energy equation. Usually, it is assumed that the internal energy of fluids is a function of the temperature uniquely, however, this is not a proper assumption for viscoelastic fluids.

Besides, the energy equation needs to be reconsidered to specify which part of the mechanical power is dissipated and which part is accumulated as elastic energy. One needs to take into account that the deformation of elastic materials is a reversible process since mechanical energy can be stored and released as mechanical energy again. Nevertheless, for purely viscous materials, the deformation is irreversible, due to mechanical energy being completely dissipated. On the contrary, for viscoelastic materials, mechanical energy will be partially stored as elastic energy and partly dissipated. This is taken into account by the stress work in the energy equation, which is computed as the product between stresses and the velocity gradient. For Newtonian fluids it is called *viscous dissipation*, as it is always positive. For viscoelastic fluids we will call it also viscous dissipation if it is positive and this property is exploited.

In literature different works can be found which study the forced convection in pipes and channels using diverse techniques, as [7, 8, 2], and more recent papers as [9] which simulate a 3D viscoelastic flow in a rectangular duct, or [10], where the application to axisymmetric 4:1 contraction flows is developed for non-isothermal flows. Also, the recirculation and thermal regions of viscoelastic flow in the symmetric planar problem for different expansion angles is studied in [11]. Moreover, the optimal control of non-isothermal viscoelastic fluids to minimize vortices and controlling the heat flux is investigated in [12] using finite differences, and also in [13], although in this case using a Newtonian flow but employing the finite element (FE) method. More recently, we found the work [14], where a 3D transient non-isothermal simulation is performed to predict the extrudate shape of viscoelastic fluids emerging from an asymmetric keyhole shaped die.

Regarding free convection examples, numerical experiments can be found in the literature that include these effects, apart from considering the contribution of the stress work into the energy equation, such as Peres et al. [15]. This work explores the significant enhancement of the convection coefficient with respect to the corresponding Newtonian fluid flow, demonstrated experimentally by Hartnett and Kostic [16]. In this case, the variation of the fluid density with temperature is dealt with in a classical way, employing the well-known Boussinesq approximation. Following similar assumptions, in [17], heat transfer is studied in a heated square cavity under the effect of thermal radiation, and [1], where the MIT benchmark 2001 [18] is carried out.

One of the main issues of such simulations, besides robustness and efficiency, is the reliability of the numerical solution. The price to be paid for enhancing the accuracy and robustness properties of such fully coupled approaches is the more expensive solution of the resulting coupled nonlinear discrete schemes.

In this work, we employ two different models to define the constitutive models, both rather similar between them. On the one hand, the Phan-Thien-Tanner (PTT) [19, 20] which is widely employed in non-isothermal fluid flows. The Oldroyd-B model is also used in this work. Also, apart from the standard viscoelastic fluid flow equations, the coupled problem is considered using the log-conformation formulation introduced first by Fattal and Kupferman in [21, 22], and applied to a FE framework using sub grid-scales in [23]. In the literature, [24] employs the log-conformation reformulation coupled with temperature to study the heat transfer enhancement by elastic turbulence in a curvy channel. Also in

[1], the thermal coupling is studied employing the log-conformation reformulation using the FE method.

The Variational Multi-scale Method has been employed to stabilize both, viscoelastic fluid flow and temperature problems. This stabilized formulation has its beginnings in the methods introduced by Hughes et al. [25] for the scalar convection-diffusion-reaction problem and later extended to the Navier-Stokes problem in [26, 27, 28], where the space of the sub-grid scales was taken as orthogonal to the FE space. This idea was adapted to the three-field Navier-Stokes problem in [29] and later to the viscoelastic flow problem in [30].

Concerning the algorithm employed, it is iterative and non-monolithic, executed in a partitioned manner. This means that in each iteration (or each time-step in the case of a time-dependent simulation) both parameters dependent of temperature in the constitutive and momentum equation and the stress work term in the energy equation are updated.

The purpose of this work is to study numerically the effect of the temperature in the viscoelastic fluid flow in two different examples using both the standard and logarithmic reformulation and a term-by-term stabilization scheme. The first example is done to validate the model in the flow past a cylinder. The second one is the 1:3 expansion, an interesting case in which the stationary solution could be asymmetric while the domain is symmetric when the Reynolds number is high enough. In the case of the patterns of viscoelastic fluids other instabilities can be activated because of the elastic component of the fluid, even in flows with low Reynolds number, resulting in a chaotic flow called elastic turbulence [31, 32, 33]. In particular, in [34], the effect in a square-square three-dimensional contraction is studied, obtaining asymmetric flows in a symmetric problem when elasticity grows. Also, in [35] the instabilities and the symmetry of the flow in a symmetric domain are analyzed for flows with high elasticity.

This paper is structured as follows. In Section 2 we present the initial and boundary problem statement, the variational form adopted, the Galerkin FE approximation, and the time discretization. Section 4 details the stabilized formulation employed for the thermal coupling. Finally, in Section 5 we present the benchmarks computed to validate the code and to explore the effect of temperature in viscoelastic fluid flows. Finally, the conclusions are summarized in Section 6.

## 2 Thermally coupled viscoelastic fluid flows

In this section, the equations that involve the coupled problem are presented, taking into account the proper modifications for both the viscoelastic fluid flow problem and the temperature problem.

### 2.1 Initial and boundary value problem

First of all we present briefly the standard equations that describe the viscoelastic fluid flow problem considering that now the different fluid parameters such as relaxation time $\lambda$ and the total viscosity $\eta_0$ have a dependency with the temperature unknown. We consider the fluid moving in a domain denoted by $\Omega \subset \mathbb{R}^d$, taking $d = 2$ or 3 depending on whether the problem is two or three dimensional. The flow takes place during the time interval $[0, T]$. The momentum, continuity, constitutive and energy equations are written as follows:

$$\rho \frac{\partial \boldsymbol{u}}{\partial t} + \rho \boldsymbol{u} \cdot \nabla \boldsymbol{u} - \nabla \cdot (2\eta_s(\vartheta) \nabla^s \boldsymbol{u}) - \nabla \cdot \boldsymbol{\sigma} + \nabla p = \boldsymbol{f} \text{ in } \Omega, t \in ]0, T[, \tag{1}$$

$$\nabla \cdot \boldsymbol{u} = 0 \text{ in } \Omega, t \in ]0, T[, \tag{2}$$

$$\frac{1}{2\eta_p(\vartheta)} (\mathbf{I} + \mathfrak{h}(\boldsymbol{\sigma})) \cdot \boldsymbol{\sigma} - \nabla^s \boldsymbol{u} + \frac{\lambda(\vartheta_0)}{2\eta_p(\vartheta_0)} \left( \frac{\partial \boldsymbol{\sigma}}{\partial t} + \boldsymbol{u} \cdot \nabla \boldsymbol{\sigma} \right)$$

$$-\frac{\lambda(\vartheta_0)}{2\eta_p(\vartheta_0)}\left(\boldsymbol{\sigma}\cdot\nabla\boldsymbol{u}+(\nabla\boldsymbol{u})^T\cdot\boldsymbol{\sigma}\right)=\mathbf{0},\ \text{in}\ \Omega,t\in]0,T[, \qquad (3)$$

$$\rho C_p\left(\frac{\partial\vartheta}{\partial t}+\boldsymbol{u}\cdot\nabla\vartheta\right)-k\Delta\vartheta-\boldsymbol{\sigma}:\nabla^s\boldsymbol{u}=0,\ \text{in}\ \Omega,t\in]0,T[, \qquad (4)$$

where $\rho$ denotes the constant density, $p:\Omega\times]0,T[\to\mathbb{R}$ is the pressure field, $\boldsymbol{u}:\Omega\times]0,T[\to\mathbb{R}^d$ is the velocity field, $\vartheta:\Omega\times]0,T[\to\mathbb{R}$ is the temperature field, $\boldsymbol{\sigma}:\Omega\times]0,T[\to\mathbb{R}^d\otimes\mathbb{R}^d$ is the viscoelastic or elastic stress tensor, $\boldsymbol{f}:\Omega\times]0,T[\to\mathbb{R}^d$ is the force field. Note that the third and fourth terms in the left-hand-side of equation (1) correspond to the divergence of the deviatoric extra stress tensor, $\boldsymbol{T}:\Omega\times]0,T[\to\mathbb{R}^d\otimes\mathbb{R}^d$, defined in terms of the viscous and the viscoelastic contribution as $\boldsymbol{T}=2\eta_s\nabla^s\boldsymbol{u}+\boldsymbol{\sigma}$.

In the energy equation (4), $C_p$ denotes the specific heat and $k$ is the thermal conductivity, considered constant.

With reference to the constitutive equation (3), $\eta_s$ represents the effective viscosity (or solvent viscosity), $\nabla^s\boldsymbol{u}$ is the symmetrical part of the velocity gradient and $\lambda$ is the relaxation time and $\eta_p$ represents the polymeric viscosity. Note that $\eta_p$, $\eta_s$ and $\lambda$ are allowed to depend on the temperature $\vartheta$, although $\lambda$ and $\eta_p$ must scale in the same way with respect to it and therefore its quotient can be evaluated with a reference temperature $\vartheta_0$ (see below). Each term of equation (3) has a particular meaning: $\nabla^s\boldsymbol{u}$ is the source, $\frac{\lambda}{2\eta_p}\boldsymbol{u}\cdot\nabla\boldsymbol{\sigma}$ represents the convective term and $\frac{\lambda}{2\eta_p}\left(\boldsymbol{\sigma}\cdot\nabla\boldsymbol{u}+(\nabla\boldsymbol{u}^T)\cdot\boldsymbol{\sigma}\right)$ are the rotational terms. Note that from this point on we will write the polymeric and the effective viscosity as a function of the total viscosity $\eta_0$. For that, an additional parameter $\beta\in[0,1]$ is introduced, so that $\eta_s=\beta\eta_0$ and $\eta_p=(1-\beta)\eta_0$. Finally, $\mathfrak{h}(\boldsymbol{\sigma})$ is a tensor that adopts different expressions depending on the constitutive equation considered. In the case of the Oldroyd-B model, tensor $\mathfrak{h}(\boldsymbol{\sigma})$ is taken as a null tensor; however for the Giesekus model [36] this tensor is equal to $\frac{\varepsilon\lambda}{\eta_p}\boldsymbol{\sigma}$, where $\varepsilon$ is the constant called *mobility factor*, and is related to the elongational behavior of the fluids and considered to be positive. Similarly, for the Phan-Thien-Tanner (PTT) model [19, 20] the tensor adopts the form $\frac{\varepsilon\lambda}{\eta_p}\mathrm{tr}\,(\boldsymbol{\sigma})\,\mathbf{I}$, where $\mathrm{tr}(\boldsymbol{\sigma})$ is the trace of the stress tensor. Note that when $\varepsilon=0$ the two models reduce to the Oldroyd-B rheological model. Also, we have to remark that, in the Giesekus and PTT models, another non-linearity is considered in the constitutive equation, defined by the product $\mathfrak{h}(\boldsymbol{\sigma})\cdot\boldsymbol{\sigma}$. This term enables a simple qualitative description of several well-known properties of viscoelastic fluids, namely, shear-thinning, the non-zero second normal stress coefficient and the stress overshoot in transient shear flows [37]. The PTT model is one of the most used approaches in the literature when non-isothermal viscoelastic fluid flow problems are addressed, and we will also consider it for some numerical computations. In [12], it is argued that the motivation of using the linearized PTT mode instead of the Oldroyd-B model is that it avoids some shortcomings when the Weissenberg number increases, due to the non-linear term discussed and a positive parameter related to the elongational behavior of the fluid which tends to lower the stresses resulting from the computations.

As it was explained in the introduction, the temperature dependence of the viscoelastic properties is defined by the principle of *time-temperature superposition*, in which that dependence is established through temperature functions. There are different functions to define accurately this relation, although the most used ones are those presented next. The first one is the Williams-Landel-Ferry (WLF) function [4], defined as follows:

$$g_{\mathrm{wlf}}(\vartheta)=\exp\left[-\frac{c_a(\vartheta-\vartheta_0)}{c_b+(\vartheta-\vartheta_0)}\right]$$

where $\vartheta_0$ is the reference temperature and $c_a$ and $c_b$ are constants. Typical extreme sets of WLF parameters ($c_a$, $c_b$) are $(5,150)$ for temperatures relatively far from the glass transition temperature $\vartheta_g$, leading to thermorheological coupling, and $(15,50)$ for

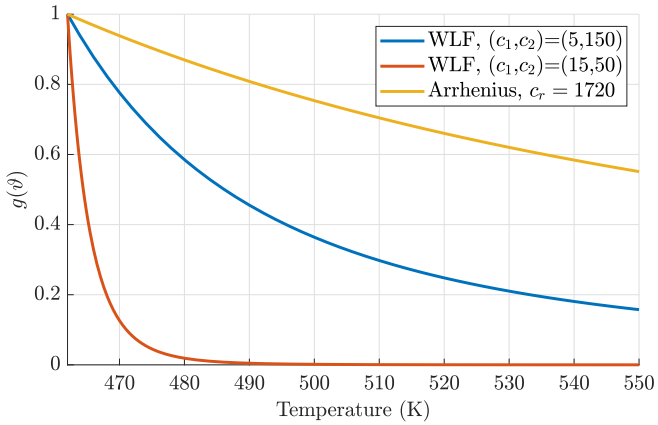


Figure 1: Comparison between different models for the temperature dependence for the viscoelastic fluid flow parameters considering $\vartheta_0 = 462$ K.

temperatures relatively close to $\vartheta_g$. The second one employed in this work is the Arrhenius function, it is given by

$$g_{\mathrm{a}}(\vartheta) = \exp\left[c_r\left(\frac{1}{\vartheta} - \frac{1}{\vartheta_0}\right)\right]$$

where in this case $c_r$ is a constant parameter and $\vartheta_0$ is the reference temperature given in Kelvin. The constant $c_r$ is considered 1720 K, as done in [38, 11]. In Figure 1 the two extreme set of parameters for the Williams-Landel-Ferry function, and the Arrhenius function considering $c_r = 1720$ K have been plot. In both functions, the temperature of reference has been fixed to 462 K to compare the shape of the curves. Note that for the WLF function, if $\vartheta_0$ is near the glass transition temperature; viscosity and relaxation time vary significantly with $\vartheta$, as it can be observed in the plots. As it was advanced in the introduction, in the work of Lomellini [6], an extensive discussion is presented about which of the two methods (WLF or Arrhenius) is more accurate, the conclusion being that the WLF approach is quite general as it applies to a lot of materials as polymer melt solutions and organic and inorganic glass-forming liquids when the temperature approaches the glass transition. However, an Arrhenius behavior is reported to better fit polyolefins and polycaprolactam liquids. To sum up, the conclusion is that the WLF model is the best representation of the data over the whole temperature range. Finally, the relation between temperature and viscoelastic properties is established as follows:

$$\lambda(\vartheta) = \lambda(\vartheta_0)g(\vartheta)$$
$$\eta_0(\vartheta) = \eta_0(\vartheta_0)g(\vartheta)$$

where $g$ is the shift factor that will be equal to $g_{\mathrm{wlf}}$ or $g_{\mathrm{a}}$ depending on the considered model, and $\lambda(\vartheta_0)$ and $\eta_0(\vartheta_0)$ are known values for the reference temperature $\vartheta_0$. Note that considering the previous expressions, in equation (3) the quotient $\frac{\lambda(\vartheta)}{\eta_0(\vartheta)}$ is a constant. Therefore, from this point we define $\Lambda(\vartheta_0)$ as $\Lambda(\vartheta_0) = \frac{\lambda(\vartheta_0)}{\eta_0(\vartheta_0)}$.

In the case of taking into account free convection, the Boussinesq approximation will be considered, adding a body force term in the momentum equation (1):

$$\gamma \boldsymbol{g}(\vartheta - \vartheta_0)$$

where $\gamma$ is the thermal expansion coefficient and $\boldsymbol{g}$ is the gravity acceleration vector.

Now, a remark about the modification in the energy equation (4) must be done. Following the work of Peters and Baaijens [2] two additional terms are considered in the

energy equations when the PTT model is considered as the constitutive equation. The energy balance equation is in this case as follows:

$$\rho C_p \left( \frac{\partial \vartheta}{\partial t} + \boldsymbol{u} \cdot \nabla \vartheta \right) - k \Delta \vartheta = \alpha \boldsymbol{\sigma} : \nabla^s \boldsymbol{u} + (1-\alpha) \frac{\mathrm{tr}(\boldsymbol{\sigma})}{2\bar{\lambda}}, \text{ in } \Omega, t \in ]0, T[$$

where $\alpha$ is a constant, and $\bar{\lambda} = \lambda \left( 1 + \frac{\lambda \varepsilon \mathrm{tr}(\boldsymbol{\sigma})}{\eta_p} \right)^{-1}$. Note that the two last terms on the right-hand side have been added to the classical energy equation, although for the case $\alpha = 1$ the standard expression would be recovered. The first term is the contribution of the entropy elasticity and the second expresses the contribution of the energy elasticity. In [2] it is argued that there are two extreme cases: $\alpha = 1$ that corresponds with the case of pure entropy elasticity and $\alpha = 0$ that is the case of pure energy elasticity. In the same work, the authors demonstrate that the effect of the parameter $\alpha$ is very small because with a fully-developed shear flow there will be no internal energy storage, and only stress work matters. Therefore, as it remarked in [15] the two $\alpha$ terms will cancel up and the final result will be mathematically equivalent to setting $\alpha = 1$, which is also argued in other works [39, 40]. Following the same arguments, in this work we will suppose that the parameter $\alpha$ is 1 in all cases. Therefore, the considered energy equation is (4). The heat source term is thus the classical one, i.e. the product between stresses and the symmetric gradient of velocities and represents the internal heat produced by internal work.

Therefore the differential equations of the initial and boundary value problem for the standard formulation are (1)-(4).

From this point, in order to distinguish operators between standard and log-conformation reformulations, we will employ the subscripts "std" and "log", respectively. Let us define $\boldsymbol{U} = [\boldsymbol{u}, p, \boldsymbol{\sigma}, \vartheta]$, $\boldsymbol{F}_{\mathrm{std}} = [\boldsymbol{f}, 0, \boldsymbol{0}, 0]$,

$$\mathcal{L}_{\mathrm{std}}(\hat{\boldsymbol{U}}; \boldsymbol{U}) := \begin{pmatrix} -\nabla \cdot \boldsymbol{\sigma} - \nabla \cdot (2\eta_s(\hat{\vartheta}) \nabla^s \boldsymbol{u}) + \rho \hat{\boldsymbol{u}} \cdot \nabla \boldsymbol{u} + \nabla p \\ \nabla \cdot \boldsymbol{u} \\ \frac{1}{2\eta_p(\hat{\vartheta})} (\mathbf{I} + \mathfrak{h}(\hat{\boldsymbol{\sigma}})) \cdot \boldsymbol{\sigma} - \nabla^s \boldsymbol{u} + \Lambda(\vartheta_0) \left( g_{\mathrm{std}}(\hat{\boldsymbol{u}}, \boldsymbol{\sigma}) \right) \\ \rho C_p \hat{\boldsymbol{u}} \cdot \nabla \vartheta - k \Delta \vartheta - \hat{\boldsymbol{\sigma}} : \nabla^s \hat{\boldsymbol{u}} \end{pmatrix} \tag{5}$$

and

$$\mathcal{D}_{\mathrm{std}} \left( \hat{\vartheta}; \boldsymbol{U} \right) := \begin{pmatrix} \rho \frac{\partial \boldsymbol{u}}{\partial t} \\ 0 \\ \frac{\lambda(\hat{\vartheta})}{2\eta_0(\hat{\vartheta})} \frac{\partial \boldsymbol{\sigma}}{\partial t} \\ \rho C_p \frac{\partial \vartheta}{\partial t} \end{pmatrix},$$

where $g_{\mathrm{std}}(\hat{\boldsymbol{u}}, \boldsymbol{\sigma}) = \hat{\boldsymbol{u}} \cdot \nabla \boldsymbol{\sigma} - \boldsymbol{\sigma} \cdot \nabla \hat{\boldsymbol{u}} - (\nabla \hat{\boldsymbol{u}})^T \cdot \boldsymbol{\sigma}$ are the convective and the rotational terms. Equations (1), (2) and (3) can be rewritten, considering $\mathcal{D}_t = \mathcal{D}_{\mathrm{std}}$, $\mathcal{L} = \mathcal{L}_{\mathrm{std}}$ and $\boldsymbol{F} = \boldsymbol{F}_{\mathrm{std}}$, as:

$$\mathcal{D}_t(\vartheta; \boldsymbol{U}) + \mathcal{L}(\boldsymbol{U}; \boldsymbol{U}) = \boldsymbol{F}. \tag{6}$$

These equations need to be completed with initial and boundary conditions to close the problem. For simplicity, we suppose the boundary condition for the velocity $\boldsymbol{u} = \boldsymbol{0}$ on $\partial\Omega$ for all time. Elastic stress conditions do not need to be prescribed. Finally, similarly to the velocity, we suppose $\vartheta = 0$ on $\partial\Omega$, in other words, we assume homogeneous Dirichlet boundary conditions for both velocity and temperature. This will allow us to simplify the writing, for example because unknowns and test functions of the variational form of the problem will belong to the same space. However, in the numerical examples we shall use

non-homogeneous boundary conditions that can be implemented as usual by shifting the unknowns with the boundary-value functions.

Regarding the initial conditions, we will set velocity, stresses and temperature to $\boldsymbol{u} = \boldsymbol{u}^0$, $\boldsymbol{\sigma} = \boldsymbol{\sigma}^0$ and $\vartheta = \vartheta^0$ at time $t = 0$ where $\boldsymbol{u}^0$, $\boldsymbol{\sigma}^0$ and $\vartheta^0$ are functions defined on the whole domain $\Omega$.

Now, we will define the set of equations in strong form for the log-conformation reformulation (see [23] for more details), taking into account the modifications considered above regarding the viscoelastic parameters and the additional term for the energy equation. The reformulation is derived basically from a change of variables, where the stress tensor is replaced by $\boldsymbol{\sigma} = \dfrac{\eta_p}{\lambda_0}(\boldsymbol{\tau} - \mathbf{I})$, and in turn, the conformation tensor $\boldsymbol{\tau}$ is written as $\boldsymbol{\tau} = \exp(\boldsymbol{\psi})$ in (1), (2) and (3). Particularly, $\lambda_0$ is linearly dependent with $\lambda$ and is defined as $\lambda_0 = \max\{k\lambda, \lambda_{0,\min}\}$, being $k$ a constant and $\lambda_{0,\min}$ a given threshold. As it is detailed in [23], in the numerical experiments we have found useful to take $k$ small, so that $\lambda_0 < \lambda$; this has allowed us to obtain converged solutions that we have not been able to get for $k = 1$. Clearly, for $k \leq 1$ we can ensure that the conformation tensor is always symmetric and positive. In the case of thermal coupling, $\lambda_0$ also depends on the temperature through the dependence with $\lambda$. Therefore, the strong form of the problem consists in finding $\boldsymbol{u}$, $p$, $\boldsymbol{\psi}$, $\vartheta$ solving the next set of equations over the domain $\Omega$ and in the interval $[0, T]$:

$$\rho\frac{\partial \boldsymbol{u}}{\partial t} - \nabla\cdot\frac{\eta_p(\vartheta)}{\lambda_0(\vartheta)}\exp(\boldsymbol{\psi}) - \nabla\cdot 2\eta_s(\vartheta)\nabla^{\mathrm{s}}\boldsymbol{u} + \rho\boldsymbol{u}\cdot\nabla\boldsymbol{u} + \nabla p = \boldsymbol{f}, \tag{7}$$

$$\nabla\cdot\boldsymbol{u} = 0, \tag{8}$$

$$\begin{aligned}\frac{1}{2\lambda_0(\vartheta)}(\exp(\boldsymbol{\psi}) - \boldsymbol{I})\cdot(\mathfrak{h}(\exp(\boldsymbol{\psi})) + \boldsymbol{I}) - \nabla^{\mathrm{s}}\boldsymbol{u} + \frac{\lambda(\vartheta)}{2\lambda_0(\vartheta)}\Big(\frac{\partial\exp(\boldsymbol{\psi})}{\partial t}\\ +\boldsymbol{u}\cdot\nabla\exp(\boldsymbol{\psi}) - \exp(\boldsymbol{\psi})\cdot\nabla\boldsymbol{u} - (\nabla\boldsymbol{u})^T\cdot\exp(\boldsymbol{\psi}) + 2\nabla^{\mathrm{s}}\boldsymbol{u}\Big) = \mathbf{0},\end{aligned} \tag{9}$$

$$\rho C_p\left(\frac{\partial\vartheta}{\partial t} + \boldsymbol{u}\cdot\nabla\vartheta\right) - k\Delta\vartheta - \left(\frac{\eta_p(\vartheta)}{\lambda_0(\vartheta)}\exp(\boldsymbol{\psi}) - \mathbf{I}\right) : \nabla^s\boldsymbol{u} = 0. \tag{10}$$

Considering again the expressions of viscoelastic parameters, we can define $\Upsilon_1(\vartheta_0) = \frac{\lambda(\vartheta_0)}{2\lambda_0(\vartheta_0)}$ and $\Upsilon_2(\vartheta_0) = \frac{\eta_p(\vartheta_0)}{\lambda_0(\vartheta_0)}$. Analogously to what was done for the standard formulation, calling $\boldsymbol{U} = [\boldsymbol{u}, p, \boldsymbol{\psi}, \vartheta]$ and $\boldsymbol{F}_{\log} = [\boldsymbol{f}, 0, \mathbf{0}, 0]$, the differential equation of the problem can be written as $\mathcal{D}_{\log}(\vartheta; \boldsymbol{U}) + \mathcal{L}_{\log}(\boldsymbol{U}; \boldsymbol{U}) = \boldsymbol{F}_{\log}$, where

$$\mathcal{L}_{\log}(\hat{\boldsymbol{U}}; \boldsymbol{U}) := \begin{pmatrix} -\nabla\cdot\Upsilon_1(\vartheta_0)\exp(\boldsymbol{\psi}) - \nabla\cdot 2\eta_s(\hat{\vartheta})\nabla^s\boldsymbol{u} + \rho\hat{\boldsymbol{u}}\cdot\nabla\boldsymbol{u} + \nabla p \\ \nabla\cdot\boldsymbol{u} \\ \dfrac{1}{2\lambda_0(\hat{\vartheta})}\left(\exp(\hat{\boldsymbol{\psi}}) - \mathbf{I}\right)\cdot(\mathfrak{h}(\exp(\boldsymbol{\psi})) + \mathbf{I}) - \nabla^s\boldsymbol{u} + \Upsilon_2(\vartheta_0)g_{\log}(\hat{\boldsymbol{u}}; \boldsymbol{u}, \boldsymbol{\psi}) \\ \rho C_p\left(\hat{\boldsymbol{u}}\cdot\nabla\vartheta\right) - k\Delta\vartheta - \left(\Upsilon_1(\vartheta_0)\exp(\hat{\boldsymbol{\psi}}) - \mathbf{I}\right) : \nabla^s\hat{\boldsymbol{u}} \end{pmatrix} \tag{11}$$

and

$$\mathcal{D}_{\log}(\boldsymbol{U}) := \begin{pmatrix} \rho\dfrac{\partial\boldsymbol{u}}{\partial t} \\ 0 \\ \Upsilon_1(\vartheta_0)\dfrac{\partial\exp(\boldsymbol{\psi})}{\partial t} \\ \rho C_p\dfrac{\partial\vartheta}{\partial t} \end{pmatrix},$$

where $g_{\log}(\hat{\boldsymbol{u}}; \boldsymbol{u}, \boldsymbol{\psi}) = \hat{\boldsymbol{u}}\cdot\nabla(\exp(\boldsymbol{\psi})) - \exp(\boldsymbol{\psi})\cdot\nabla\hat{\boldsymbol{u}} - (\nabla\hat{\boldsymbol{u}})^T\cdot\exp(\boldsymbol{\psi}) + 2\nabla^s\boldsymbol{u}$ are the convective and rotational terms.

In this case the boundary and initial conditions are similar to the ones described above, but now instead of $\boldsymbol{\sigma}$ we have the dimensionless tensor $\boldsymbol{\psi}$, which will adopt the value $\boldsymbol{\psi} = \boldsymbol{\psi}^0$ at time $t = 0$.

## 2.2 Variational form

Let us introduce some specific notation in order to define the weak form of the viscoelastic problem: $L^2(\omega)$ is the space of square integrable functions in a domain $\omega$ while $H^m(\omega)$ is the space of functions whose distributional derivatives of order up to $m \geq 0$ (integer) belong to $L^2(\omega)$. The norm in a space $X$ is denoted by $\|\cdot\|_X$, except in the case $X = L^2(\Omega)$, where the subscript is omitted. The space $H_0^1(\omega)$ comprises functions in $H^1(\omega)$ vanishing on $\partial\omega$ and $H^{-1}(\Omega)$ is the topological dual of $H_0^1(\Omega)$, the duality pairing being $\langle\cdot,\cdot\rangle$. Finally, the $L^2$ inner product in $\omega$ (for scalars, vectors and tensors) is denoted by $(\cdot,\cdot)_\omega$ and the integral over $\omega$ of the product of two general functions is written as $\langle\cdot,\cdot\rangle_\omega$ (the subscript being omitted when $\omega = \Omega$).

Using this notation, velocity, pressure and stress FE spaces for the continuous problem are: $\boldsymbol{V}_0 = H_0^1(\Omega)^d$ for the velocity, $\mathcal{Q} = L^2(\Omega)/\mathbb{R}$ for the pressure, $\boldsymbol{\Upsilon} = H^1(\Omega)^{d\times d}_{\text{sym}}$ for the stresses in the standard formulation (the subscript standing for symmetric tensors), and for the temperature $\mathcal{T} = H_0^1(\Omega)$ for each fixed time $t$. Therefore, the weak form of the coupled for the standard formulation problem consists in finding $\boldsymbol{U} = [\boldsymbol{u}, p, \boldsymbol{\sigma}, \vartheta]$ $:]0,T[\longrightarrow \boldsymbol{\mathcal{X}} := \boldsymbol{V}_0 \times \boldsymbol{Q} \times \boldsymbol{\Upsilon} \times \mathcal{T}$, such that the initial conditions are satisfied and:

$$\begin{aligned}
\left(\rho\frac{\partial \boldsymbol{u}}{\partial t}, \boldsymbol{v}\right) + (\boldsymbol{\sigma}, \nabla^s \boldsymbol{v}) + 2(\eta_s(\vartheta)\nabla^s \boldsymbol{u}, \nabla^s \boldsymbol{v}) + \langle \rho \boldsymbol{u}\cdot\nabla\boldsymbol{u}, \boldsymbol{v}\rangle - (p, \nabla\cdot\boldsymbol{v}) &= \langle \boldsymbol{f}, \boldsymbol{v}\rangle,\\
(q, \nabla\cdot\boldsymbol{u}) &= 0,\\
\left(\frac{1}{2\eta_p(\vartheta)}(\mathbf{I} + \mathfrak{h}(\boldsymbol{\sigma}))\cdot\boldsymbol{\sigma}, \boldsymbol{\chi}\right) - (\nabla^s\boldsymbol{u}, \boldsymbol{\chi}) + \Lambda(\vartheta_0)\left(\frac{\partial\boldsymbol{\sigma}}{\partial t} + \boldsymbol{u}\cdot\nabla\boldsymbol{\sigma}, \boldsymbol{\chi}\right)&\\
-\Lambda(\vartheta_0)\left(\boldsymbol{\sigma}\cdot\nabla\boldsymbol{u} + (\nabla\boldsymbol{u})^T\cdot\boldsymbol{\sigma}, \boldsymbol{\chi}\right) &= 0,\\
\rho C_p\left(\frac{\partial\vartheta}{\partial t} + \boldsymbol{u}\cdot\nabla\vartheta, \xi\right) + (k\nabla\vartheta, \nabla\xi) - (\boldsymbol{\sigma} : \nabla^s\boldsymbol{u}, \xi) &= 0,
\end{aligned}$$

for all $\boldsymbol{V} = [\boldsymbol{v}, q, \boldsymbol{\chi}, \xi] \in \boldsymbol{\mathcal{X}}$. In compact form, the problem can be written as:

$$\mathcal{G}_{\text{std}}(\boldsymbol{U}, \boldsymbol{V}) + B_{\text{std}}(\boldsymbol{U}; \boldsymbol{U}, \boldsymbol{V}) = L_{\text{std}}(\boldsymbol{V}), \tag{12}$$

for all $\boldsymbol{V} \in \boldsymbol{\mathcal{X}}$, where

$$\mathcal{G}_{\text{std}}(\boldsymbol{U}, \boldsymbol{V}) = \left(\rho\frac{\partial\boldsymbol{u}}{\partial t}, \boldsymbol{v}\right) + \Lambda(\vartheta_0)\left(\frac{\partial\boldsymbol{\sigma}}{\partial t}, \boldsymbol{\chi}\right) + \rho C_p\left(\frac{\partial\vartheta}{\partial t}, \xi\right), \tag{13}$$

$$\begin{aligned}
B_{\text{std}}(\hat{\boldsymbol{U}}; \boldsymbol{U}, \boldsymbol{V}) =& 2(\eta_s(\hat{\vartheta})\nabla^s\boldsymbol{u}, \nabla^s\boldsymbol{v}) + \langle\rho\hat{\boldsymbol{u}}\cdot\nabla\boldsymbol{u}, \boldsymbol{v}\rangle + (\boldsymbol{\sigma}, \nabla^s\boldsymbol{v})\\
&- (p, \nabla\cdot\boldsymbol{v}) + (q, \nabla\cdot\boldsymbol{u}) + \left(\frac{1}{2\eta_p(\hat{\vartheta})}(\mathbf{I} + \mathfrak{h}(\hat{\boldsymbol{\sigma}}))\cdot\boldsymbol{\sigma}, \boldsymbol{\chi}\right)\\
&- (\nabla^s\boldsymbol{u}, \boldsymbol{\chi}) + \Lambda(\vartheta_0)\left(\hat{\boldsymbol{u}}\cdot\nabla\boldsymbol{\sigma} - \boldsymbol{\sigma}\cdot\nabla\hat{\boldsymbol{u}} - (\nabla\hat{\boldsymbol{u}})^T\cdot\boldsymbol{\sigma}, \boldsymbol{\chi}\right)\\
&+ \rho C_p\left(\hat{\boldsymbol{u}}\cdot\nabla\vartheta, \xi\right) + (k\nabla\vartheta, \nabla\xi) - \left(\hat{\boldsymbol{\sigma}} : \nabla^s\hat{\boldsymbol{u}}, \xi\right),
\end{aligned} \tag{14}$$

$$L_{\text{std}}(\boldsymbol{V}) = \langle\boldsymbol{f}, \boldsymbol{v}\rangle. \tag{15}$$

Analogously, considering now the logarithmic reformulation of the viscoelastic flow problem, the spaces for the velocity, pressure and temperature for the continuous problems are the ones defined above for the standard formulation. However, now the space for tensor $\boldsymbol{\psi}$ is denoted by $\bar{\boldsymbol{\Upsilon}}$ for each fixed time $t$, where an appropriate regularity is assumed (see [23]). So, in this case the weak form of the problem consists in finding $\boldsymbol{U} = [\boldsymbol{u}, p, \boldsymbol{\psi}, \vartheta]$ :

$]0,T[\longrightarrow \bar{\boldsymbol{\mathcal{X}}} := \boldsymbol{V}_0 \times \mathcal{Q} \times \bar{\boldsymbol{\Upsilon}} \times \mathcal{T}$, such that the initial conditions are satisfied and for all $\boldsymbol{V} = [\boldsymbol{v}, q, \boldsymbol{\chi}, \xi] \in \boldsymbol{\mathcal{X}}$,

$$\mathcal{G}_{\log}(\vartheta; \boldsymbol{U}, \boldsymbol{V}) + B_{\log}(\boldsymbol{U}; \boldsymbol{U}, \boldsymbol{V}) = L_{\log}(\vartheta; \boldsymbol{V}), \tag{16}$$

where each term is defined as

$$\mathcal{G}_{\log}(\hat{\vartheta}; \boldsymbol{U}, \boldsymbol{V}) = \left(\rho \frac{\partial \boldsymbol{u}}{\partial t}, \boldsymbol{v}\right) + \left(\Upsilon_1(\vartheta_0) \frac{\partial \exp(\boldsymbol{\psi})}{\partial t}, \boldsymbol{\chi}\right) + \rho C_p \left(\frac{\partial \vartheta}{\partial t}, \xi\right), \tag{17}$$

$$\begin{aligned} B_{\log}(\hat{\boldsymbol{U}}; \boldsymbol{U}, \boldsymbol{V}) = {} & (\Upsilon_2(\vartheta_0) \exp(\boldsymbol{\psi}), \nabla^s \boldsymbol{v}) + 2(\eta_s(\hat{\vartheta}) \nabla^s \boldsymbol{u}, \nabla^s \boldsymbol{v}) + \langle \rho \hat{\boldsymbol{u}} \cdot \nabla \boldsymbol{u}, \boldsymbol{v} \rangle \\ & - (p, \nabla \cdot \boldsymbol{v}) + (\nabla \cdot \boldsymbol{u}, q) + \left(\frac{1}{2\lambda_0(\hat{\vartheta})} (\exp(\boldsymbol{\psi} - \mathbf{I})) \cdot \left(\mathfrak{h}(\exp(\hat{\boldsymbol{\psi}})) + \mathbf{I}\right), \boldsymbol{\chi}\right) \\ & - (\nabla^s \boldsymbol{u}, \boldsymbol{\chi}) + (\Upsilon_1(\vartheta_0) (\hat{\boldsymbol{u}} \cdot \nabla \exp(\boldsymbol{\psi}) - \exp(\boldsymbol{\psi}) \cdot \nabla \hat{\boldsymbol{u}}), \boldsymbol{\chi}) \\ & - \left(\Upsilon_1(\vartheta_0) \left((\nabla \hat{\boldsymbol{u}})^T \cdot \exp(\boldsymbol{\psi}) - 2\nabla^s \boldsymbol{u}\right), \boldsymbol{\chi}\right) \\ & + \rho C_p (\hat{\boldsymbol{u}} \cdot \nabla \vartheta, \xi) + (k \nabla \vartheta, \nabla \xi) - \left(\Upsilon_2(\vartheta_0) \left(\exp(\hat{\boldsymbol{\psi}}) - \mathbf{I} : \nabla^s \hat{\boldsymbol{u}}\right), \xi\right), \end{aligned} \tag{18}$$

$$L_{\log}(\hat{\vartheta}; \boldsymbol{V}) = \langle \boldsymbol{f}, \boldsymbol{v} \rangle. \tag{19}$$

Note that the space of the test functions is the same as for the standard formulation, i.e., the change of variables is made for the stress unknown, but not for the stress test function.

For the coupled problem, we have to consider several dimensionless numbers to characterize the problem. On the one hand, we have the Reynolds number, which comes from the Navier-Stokes equations and relates inertial and viscous forces. Secondly, we have the Weissenberg number, a dimensionless number essential to characterize viscoelastic fluid flow problems. This, as it was already defined, indicates the relevance of the elastic terms of the constitutive equation, and compares elastic forces with viscous forces. Regarding the dimensionless number associated with the energy equation, we have selected the Prandtl number, which relates transport with thermal diffusivity. Finally, we need a global dimensionless number able to describe how strong is the coupling between the fluid flow and the temperature model. With this finality, we consider the Brinkman number, which compares the inertial power with the heat conduction. Therefore we have a total of four dimensionless number to define each coupled problem:

$$\begin{array}{llll} \text{Reynolds number:} & \mathrm{Re} = \dfrac{\rho L U}{\eta_0}, & \text{Prandtl number:} & \mathrm{Pr} = \dfrac{\eta_0 C_p}{k_f}, \\ \text{Weissenberg number:} & \mathrm{We} = \dfrac{\lambda U}{L}, & \text{Brinkman number:} & \mathrm{Br} = \dfrac{\eta_0 U^2}{k_f (\vartheta_w - \vartheta_i)}, \end{array}$$

where $L$ is the characteristic length, $U$ the characteristic velocity of the problem, $\vartheta_w$ is the temperature on a reference wall and $\vartheta_i$ is the temperature at the inflow. The remaining parameters that appear in the previous expressions are properties that correspond to the viscoelastic fluid flow problem or the temperature problem, and which are explained in the previous sections.

# 3 Galerkin finite element discretization and time discretization

Once the variational problems for both formulations (12) and (16) have been defined, the Galerkin approximation can be established. The FE partition of the domain $\Omega$ is denoted by $\mathcal{P}_h = \{K\}$. Likewise, the diameter of an element $K \in \mathcal{P}_h$ is denoted by $h_K$ and the diameter of the partition is defined as $h = \max\{h_K | K \in \mathcal{P}_h\}$.

So, for the standard formulation, from $\mathcal{P}_h$ we may construct conforming FE spaces for the velocity, the pressure, the elastic stress and the temperature, $\boldsymbol{\mathcal{V}}_h \subset \boldsymbol{\mathcal{V}}$, $\mathcal{Q}_h \subset \mathcal{Q}$, $\boldsymbol{\Upsilon}_h \subset \boldsymbol{\Upsilon}$ and $\mathcal{T}_h \subset \mathcal{T}$, respectively. Calling $\boldsymbol{\mathcal{X}}_h := \boldsymbol{\mathcal{V}}_h \times \mathcal{Q}_h \times \boldsymbol{\Upsilon}_h \times \mathcal{T}_h$, the Galerkin FE approximation of the problem consists in finding $\boldsymbol{U}_h : ]0,T[ \longrightarrow \boldsymbol{\mathcal{X}}_h$, such that:

$$\mathcal{G}_{\text{std}}(\vartheta_h; \boldsymbol{U}_h, \boldsymbol{V}_h) + B_{\text{std}}(\boldsymbol{U}_h; \boldsymbol{U}_h, \boldsymbol{V}_h) = L_{\text{std}}(\boldsymbol{V}_h),$$

for all $\boldsymbol{V}_h = [\boldsymbol{v}_h, q_h, \boldsymbol{\chi}_h, \xi_h] \in \boldsymbol{\mathcal{X}}_h$, and satisfying the appropriate initial conditions.

Now, for the logarithmic conformation reformulation, from $\mathcal{T}_h$ we construct the FE space for the new variable $\boldsymbol{\psi}$, $\bar{\boldsymbol{\Upsilon}}_h \subset \bar{\boldsymbol{\Upsilon}}$. $\bar{\boldsymbol{\mathcal{X}}}_h := \boldsymbol{\mathcal{V}}_h \times \mathcal{Q}_h \times \bar{\boldsymbol{\Upsilon}}_h \times \mathcal{T}_h$ is the Galerkin FE space now, and the Galerkin approximation consists in finding $\boldsymbol{U}_h : ]0,T[ \longrightarrow \bar{\boldsymbol{\mathcal{X}}}_h$, such that

$$\mathcal{G}_{\log}(\vartheta_h; \boldsymbol{U}_h, \boldsymbol{V}_h) + B_{\log}(\boldsymbol{U}_h; \boldsymbol{U}_h, \boldsymbol{V}_h) = L_{\log}(\vartheta_h; \boldsymbol{V}_h),$$

for all $\boldsymbol{V}_h = [\boldsymbol{v}_h, q_h, \boldsymbol{\chi}_h, \xi_h] \in \boldsymbol{\mathcal{X}}_h$. We have to remark that the Galerkin approximation is not enough to obtain a stable formulation unless convective terms are not relevant and the appropriate compatibility conditions on the FE spaces hold. Therefore, the next section presents a stable formulation.

Regarding the time discretization in this paper the backward differencing (BDF) scheme is considered, in particular BDF1. The first order scheme is not the best discretization to capture time-dependent responses. However, the numerical examples presented in this paper have a steady-state solution, and therefore a BDF1 scheme with a uniform partition of size $\delta t$ will be suitable in these cases. The time step level will be denoted with a superscript.

Moreover, for the log-conformation reformulation we need to obtain the linearized expression for the time derivative of the exponential as follows (see [23]):

$$\begin{aligned}\left.\frac{\partial \exp(\boldsymbol{\psi})}{\partial t}\right|_{t^{n+1}} = \frac{1}{\delta t}\Big[&\exp(\hat{\boldsymbol{\psi}}^{n+1}) \cdot \boldsymbol{\psi}^{n+1} + \exp(\hat{\boldsymbol{\psi}}^{n+1}) - \exp(\hat{\boldsymbol{\psi}}^{n+1}) \cdot \hat{\boldsymbol{\psi}}^{n+1} \\ &- \exp(\boldsymbol{\psi}^{n})\Big] + \mathcal{O}\left(\delta t\right) + \mathcal{O}\left(\left(\delta \boldsymbol{\psi}^{n+1}\right)^2\right),\end{aligned}$$

where $\hat{\boldsymbol{\psi}}^{n+1}$ stands for a previous guess of $\boldsymbol{\psi}^{n+1}$ that depends on the linearization scheme and $\delta\boldsymbol{\psi}^{n+1} = \boldsymbol{\psi}^{n+1} - \hat{\boldsymbol{\psi}}^{n+1}$.

# 4 Stabilized finite element formulation

In this section, we will describe briefly the stabilized formulation employed for the thermal coupling. For both formulations, standard and logarithmic, the stabilization used departs from the Variational Multi-Scale (VMS) method, widely described in [25]. The method consists in splitting the unknowns $\boldsymbol{U}$ into two different parts: the component that is computed by the FE space, denoted by $\boldsymbol{U}_h$ and the part that cannot be solved by the FE space, called sub-grid scale and which is denoted by $\tilde{\boldsymbol{U}}$. The stabilized method employed in this paper is analogous to the one presented in [29] for the standard formulation and the one presented in [23] for the log-conformation reformulation for the viscoelastic fluid flow. As the main ideas of the stabilization method have been already presented previously, in this section we restrict us to the extension to the thermal coupling.

## 4.1 Residual-based VMS methods

Firstly, we present the case of the standard formulation. Suppose that $\mathcal{L}_{\text{std}}(\hat{\boldsymbol{U}}; \cdot)$ is a linear operator for a given $\hat{\boldsymbol{U}} = [\hat{\boldsymbol{u}}, \hat{p}, \hat{\boldsymbol{\sigma}}, \hat{\vartheta}]$ known. Introducing the sub-grid scale, and

integrating by parts, the method consists in finding $\boldsymbol{U}_h : ]0,T[ \longrightarrow \boldsymbol{\mathcal{X}}_h$, such that

$$\mathcal{G}_{\text{std}}(\vartheta_h;\boldsymbol{U}_h,\boldsymbol{V}_h)+B_{\text{std}}(\boldsymbol{U}_h;\boldsymbol{U}_h,\boldsymbol{V}_h)+\sum_K\langle\tilde{\boldsymbol{U}},\mathcal{L}^*(\boldsymbol{U}_h;\boldsymbol{V}_h)\rangle_K=L_{\text{std}}(\boldsymbol{V}_h), \tag{20}$$

for all $\boldsymbol{V}_h \in \boldsymbol{\mathcal{X}}_h$, where $\mathcal{L}^*(\hat{\boldsymbol{U}};\cdot)$ is the formal adjoint of $\mathcal{L}_{\text{std}}(\hat{\boldsymbol{U}};\cdot)$, typically without considering boundary conditions, $\tilde{\boldsymbol{U}}$ is the sub-grid scale, which needs to be approximated and has components $\tilde{\boldsymbol{U}}=\left[\tilde{\boldsymbol{u}},\tilde{p},\tilde{\boldsymbol{\sigma}},\tilde{\vartheta}\right]$. All approximations have been considered continuous; in this case expression (20) is justified in [41]. Similarly, for the log-conformation reformulation, we have to find $\boldsymbol{U}_h : ]0,T[ \longrightarrow \tilde{\boldsymbol{\mathcal{X}}}_h$ such that

$$\mathcal{G}_{\log}(\vartheta_h;\boldsymbol{U}_h,\boldsymbol{V}_h)+B_{\log}(\boldsymbol{U}_h;\boldsymbol{U}_h,\boldsymbol{V}_h)+\sum_K\langle\tilde{\boldsymbol{U}},\mathcal{L}^*(\boldsymbol{U}_h;\boldsymbol{V}_h)\rangle_K=L_{\log}(\vartheta_h;\boldsymbol{V}_h), \tag{21}$$

for all $\boldsymbol{V}_h \in \boldsymbol{\mathcal{X}}_h$. Let us remark that for both formulations (standard and logarithmic) the same operator $\mathcal{L}^*\left(\hat{\boldsymbol{U}};\boldsymbol{V}\right)$ is used:

$$\mathcal{L}^*(\hat{\boldsymbol{U}};\boldsymbol{V}):=\begin{pmatrix}\nabla\cdot\boldsymbol{\chi}-(\hat{\vartheta})\nabla\cdot(2\eta_s\nabla^s\boldsymbol{v})-\rho\hat{\boldsymbol{u}}\cdot\nabla\boldsymbol{v}-\nabla q\\ -\nabla\cdot\boldsymbol{v}\\ \dfrac{1}{2\eta_p(\hat{\vartheta})}\left(\mathbf{I}+\mathfrak{h}(\hat{\boldsymbol{\sigma}})\right)\cdot\boldsymbol{\chi}+\nabla^s\boldsymbol{v}-\Lambda(\vartheta_0)\left(\hat{\boldsymbol{u}}\cdot\nabla\boldsymbol{\chi}+g^*(\hat{\boldsymbol{u}},\boldsymbol{\chi})\right)\\ \rho C_p\hat{\boldsymbol{u}}\cdot\nabla\xi-k\Delta\xi\end{pmatrix}, \tag{22}$$

where in this case $g^*(\hat{\boldsymbol{u}},\boldsymbol{\chi})=\boldsymbol{\chi}\cdot(\nabla\hat{\boldsymbol{u}})^T+\boldsymbol{\chi}\cdot\nabla\hat{\boldsymbol{u}}$. As the operators $\mathcal{D}_t$ and $\mathcal{L}$ were defined previously for both formulations, the sub-grid scales can be written in terms of the finite element component:

$$\tilde{\boldsymbol{U}}=\boldsymbol{\alpha}\tilde{P}[\boldsymbol{F}-\mathcal{D}_t(\vartheta_h;\boldsymbol{U}_h)-\mathcal{L}(\boldsymbol{U}_h;\boldsymbol{U}_h)], \tag{23}$$

where we denote as $\tilde{P}$ the $L^2$ projection onto the space of sub-grid scales. The ASGS (Algebraic Sub-Grid Scales) method is recovered if $\tilde{P}$ is the projection onto the space of FE residuals; however if $\tilde{P}$ is taken as the orthogonal projection to the FE space, $P^{\perp}$, then the OSGS (Orthogonal Sub-Grid Scales) method would be recovered.

Regarding matrix $\boldsymbol{\alpha}$ that appears in expression (23), it is the diagonal matrix of stabilization terms, $\boldsymbol{\alpha}=\text{diag}(\alpha_1\boldsymbol{I}_d,\alpha_2,\alpha_3\boldsymbol{I}_{d\times d},\alpha_4)$ with $\boldsymbol{I}_d$ the identity on vectors of $\mathbb{R}^d$, $\boldsymbol{I}_{d\times d}$ the identity on second order tensors and the parameters $\alpha_i$, $i=1,2,3,4$ are computed as

$$\alpha_1=\left[c_1\frac{\eta_0(\vartheta_h)}{h_1^2}+c_2\frac{\rho|\boldsymbol{u}_h|}{h_2}\right]^{-1}, \tag{24}$$

$$\alpha_2=\frac{h_1^2}{c_1\alpha_1}, \tag{25}$$

$$\alpha_3=\left[c_3\frac{1}{2\eta_p(\vartheta_h)}+c_4\Lambda(\vartheta_0)\left(\frac{|\boldsymbol{u}_h|}{h_2}+|\nabla\boldsymbol{u}_h|\right)\right]^{-1}, \tag{26}$$

$$\alpha_4=\left[c_5\frac{k}{h_1^2}+c_6\frac{\rho C_p|\boldsymbol{u}_h|}{h_2}\right]^{-1}, \tag{27}$$

where $c_i$ with $i=1,..,6$ are constants, $h_1$ is the characteristic length computed as the square root of the element area or the cubic root of the element volume depending on the dimension of the case, and $h_2$ is another characteristic length computed as the element length in the streamline direction (see [42] for more details). The constants $c_i, i=1,..,6$ are algorithmic parameters in the formulation. The values employed in this paper for the numerical simulations are: $c_1=4.0$, $c_2=1.0$, $c_3=4.0$, $c_4=0.25$, $c_5=12.0$ and $c_6=2.0$. We keep these values constants for all flows.

Inserting (23) in (20) for the standard formulation, with $\boldsymbol{\alpha}$ given above and using the adjoint operator (22), we obtain the following problem: find $\boldsymbol{U}_h : ]0,T[ \longrightarrow \boldsymbol{\mathcal{X}}_h$ such that

$$(\mathcal{G}_{\text{std}}(\vartheta_h;\boldsymbol{U}_h),\boldsymbol{V}_h) + B_{\text{std}}(\boldsymbol{U}_h;\boldsymbol{U}_h,\boldsymbol{V}_h) + S_{1,\text{std}}(\boldsymbol{u}_h,\vartheta_h;\boldsymbol{U}_h,\boldsymbol{V}_h) + S_2(\boldsymbol{U}_h,\boldsymbol{V}_h) + S_{3,\text{std}}(\boldsymbol{U}_h;\boldsymbol{U}_h,\boldsymbol{V}_h) + S_{4,\text{std}}(\boldsymbol{u}_h,\boldsymbol{\sigma}_h;\boldsymbol{U}_h,\boldsymbol{V}_h) = L_{\text{std}}(\boldsymbol{V}_h) + R_{1,\text{std}}\left(\boldsymbol{u}_h,\vartheta_h;\boldsymbol{V}_h\right), \quad (28)$$

for all $\boldsymbol{V}_h \in \boldsymbol{\mathcal{X}}_h$. The details of each stabilized term can be found in the work of Castillo and Codina [29], with exception of the expression $S_{4,\text{std}}$, which corresponds to stabilization terms of the energy equation. These terms are:

$$\begin{aligned} S_{1,\text{std}}\left(\hat{\boldsymbol{u}}_h,\hat{\vartheta}_h;\boldsymbol{U}_h,\boldsymbol{V}_h\right) = \sum_K \alpha_1 \Big\langle \tilde{P}\Big[\rho\frac{\partial \boldsymbol{u}_h}{\partial t} - \nabla\cdot\boldsymbol{\sigma}_h - \nabla\cdot 2\eta_s(\hat{\vartheta}_h)\nabla^{\text{s}}\boldsymbol{u}_h \\ +\rho\hat{\boldsymbol{u}}_h\cdot\nabla\boldsymbol{u}_h + \nabla p_h\Big], \\ -\nabla\cdot\boldsymbol{\chi}_h + \nabla\cdot 2\eta_s(\hat{\vartheta}_h)\nabla^s\boldsymbol{v}_h + \rho\hat{\boldsymbol{u}}_h\cdot\nabla\boldsymbol{v}_h + \nabla q_h\Big\rangle_K, \quad (29) \end{aligned}$$

$$S_2\left(\boldsymbol{U}_h,\boldsymbol{V}_h\right) = \sum_K \alpha_2 \left\langle \tilde{P}\left[\nabla\cdot\boldsymbol{u}_h\right], \nabla\cdot\boldsymbol{v}_h\right\rangle_K, \quad (30)$$

$$\begin{aligned} S_{3,\text{std}}\left(\hat{\boldsymbol{U}}_h;\boldsymbol{U}_h,\boldsymbol{V}_h\right) = \sum_K \alpha_3 \Big\langle \tilde{P}\Big[\frac{1}{2\eta_p(\hat{\vartheta}_h)}\left(\mathbf{I}+\mathfrak{h}(\hat{\boldsymbol{\sigma}}_h)\right)\boldsymbol{\sigma}_h - \nabla^s\boldsymbol{u}_h \\ +\Lambda(\vartheta_0)\left(\frac{\partial\boldsymbol{\sigma}_h}{\partial t} + g_{\text{std}}(\hat{\boldsymbol{u}}_h;\boldsymbol{\sigma}_h)\right)\Big], \\ -\frac{1}{2\eta_p(\hat{\vartheta}_h)}\left(\mathbf{I}+\mathfrak{h}(\hat{\boldsymbol{\sigma}}_h)\right)\cdot\boldsymbol{\chi}_h - \nabla^s\boldsymbol{v}_h \\ +\Lambda(\vartheta_0)\left(\hat{\boldsymbol{u}}_h\cdot\nabla\boldsymbol{\chi}_h + g^*(\hat{\boldsymbol{u}}_h,\boldsymbol{\chi}_h)\right)\rangle_K, \quad (31) \end{aligned}$$

$$\begin{aligned} S_{4,\text{std}}\left(\hat{\boldsymbol{u}}_h,\hat{\boldsymbol{\sigma}}_h;\boldsymbol{U}_h,\boldsymbol{V}_h\right) = \sum_K \alpha_4 \Big\langle \tilde{P}\Big[\rho C_p\left(\frac{\partial\vartheta_h}{\partial t} + \hat{\boldsymbol{u}}_h\cdot\nabla\vartheta_h\right) - k\Delta\vartheta_h - \hat{\boldsymbol{\sigma}}_h : \nabla^s\hat{\boldsymbol{u}}_h\Big], \\ -\rho C_p\hat{\boldsymbol{u}}_h\cdot\nabla\xi_h + k\Delta\xi_h\rangle_K, \quad (32) \end{aligned}$$

$$\begin{aligned} R_{1,\text{std}}\left(\hat{\boldsymbol{u}}_h,\hat{\vartheta}_h;\boldsymbol{V}_h\right) = \sum_K \alpha_1 \Big\langle \tilde{P}\left[\boldsymbol{f}\right], -\nabla\cdot\boldsymbol{\chi}_h + \nabla\cdot 2\eta_s(\hat{\vartheta}_h)\nabla^s\boldsymbol{v}_h \\ +\rho\hat{\boldsymbol{u}}_h\cdot\nabla\boldsymbol{v}_h + \nabla q_h\rangle_K. \quad (33) \end{aligned}$$

Recall that if $\tilde{P} = I$ we obtain the ASGS method, and if $\tilde{P} = P_h^{\perp} = I - P_h$ the we would be considering the OSGS method.

Analogously, in the case of the stabilization formulation for the logarithmic case, inserting (23) in (21) and using the adjoint operator defined in (22), we obtain the following problem: find $\boldsymbol{U}_h : ]0,T[ \longrightarrow \boldsymbol{\mathcal{X}}_h$ such that

$$(\mathcal{G}_{\log}(\vartheta_h;\boldsymbol{U}_h),\boldsymbol{V}_h) + B_{\log}(\boldsymbol{U}_h;\boldsymbol{U}_h,\boldsymbol{V}_h) + S_{1,\log}(\boldsymbol{u}_h,\vartheta_h;\boldsymbol{U}_h,\boldsymbol{V}_h) + S_2(\boldsymbol{U}_h,\boldsymbol{V}_h) + S_{3,\log}(\boldsymbol{U}_h;\boldsymbol{U}_h,\boldsymbol{V}_h) + S_{4,\log}(\boldsymbol{U}_h;\boldsymbol{U}_h,\boldsymbol{V}_h) = L_{\log}(\boldsymbol{V}_h) + R_{1,\log}\left(\boldsymbol{u}_h,\vartheta_h;\boldsymbol{V}_h\right). \quad (34)$$

In this case, $S_{i,\log}$, with $i = 1,2,3$ and $R_{j,\log}$ with $j = 1,3$ are detailed in [23] and the only difference is that now we have to consider the temperature-dependence of the viscoelastic variables. These terms are

$$\begin{aligned} S_{1,\log}(\hat{\boldsymbol{u}}_h,\hat{\vartheta}_h;\boldsymbol{U}_h,\boldsymbol{V}_h) = \sum_K \alpha_1 \Big\langle \tilde{P}\Big[\rho\frac{\partial\boldsymbol{u}_h}{\partial t} - \nabla\cdot\left(\Upsilon_2(\vartheta_0)\exp(\boldsymbol{\psi}_h)\right) - \nabla\cdot\left(2\eta_s(\hat{\vartheta})\nabla^s\boldsymbol{u}_h\right) \\ +\rho\hat{\boldsymbol{u}}_h\cdot\nabla\boldsymbol{u}_h + \nabla p_h\Big], \\ -\nabla\cdot\boldsymbol{\chi}_h + \nabla\cdot\left(2\eta_s(\hat{\vartheta}_h)\nabla^s\boldsymbol{v}_h\right) + \rho\hat{\boldsymbol{u}}_h\cdot\nabla\boldsymbol{v}_h + \nabla q_h\Big\rangle_K, \quad (35) \end{aligned}$$

$$S_{2,\log}(\boldsymbol{U}_h,\boldsymbol{V}_h)=\sum_K \alpha_2\Big\langle \tilde{P}[\nabla\cdot\boldsymbol{u}_h],\nabla\cdot\boldsymbol{v}_h\Big\rangle_K, \tag{36}$$

$$\begin{aligned}S_{3,\log}(\hat{\boldsymbol{u}}_h,\hat{\vartheta}_h;\boldsymbol{U}_h,\boldsymbol{V}_h)=\sum_K \alpha_3\Big\langle \tilde{P}\Big[&\frac{1}{2\lambda_0(\hat{\vartheta}_h)}\left(\exp(\boldsymbol{\psi}_h)-\mathbf{I}\right)\cdot\left(\mathfrak{h}(\exp(\boldsymbol{\psi}_h))+\mathbf{I}\right)-\nabla^s\boldsymbol{u}_h\\ &+\Upsilon_1(\vartheta_0)\Big(\frac{\partial\exp(\boldsymbol{\psi}_h)}{\partial t}+g_{\log}(\hat{\boldsymbol{u}}_h;\boldsymbol{u}_h,\boldsymbol{\psi}_h)\Big)\Big],\\ &-\frac{1}{2\eta_p(\hat{\vartheta}_h)}\boldsymbol{\chi}_h-\nabla^s\boldsymbol{v}_h+\Upsilon_2(\vartheta_0)\left(\hat{\boldsymbol{u}}_h\cdot\nabla\boldsymbol{\chi}_h+g^*(\hat{\boldsymbol{u}}_h,\boldsymbol{\chi}_h)\right)\Big\rangle_K,\end{aligned} \tag{37}$$

$$R_{1,\log}(\hat{\boldsymbol{u}}_h,\hat{\vartheta}_h;\boldsymbol{V}_h)=\sum_K \alpha_1\Big\langle \tilde{P}\Big[\boldsymbol{f}\Big],-\nabla\cdot\boldsymbol{\chi}_h+\nabla\cdot(2\eta_s(\hat{\vartheta}_h)\nabla^s\boldsymbol{v}_h)+\rho\hat{\boldsymbol{u}}_h\cdot\nabla\boldsymbol{v}_h+\nabla q_h\Big\rangle_K. \tag{38}$$

Regarding $S_{4,\log}$, it is as follows:

$$\begin{aligned}S_{4,\log}\left(\hat{\boldsymbol{U}}_h;\boldsymbol{U}_h,\boldsymbol{V}_h\right)=\sum_K \alpha_4\Big\langle \tilde{P}\,[&\rho C_p\hat{\boldsymbol{u}}_h\cdot\nabla\vartheta_h-k\Delta\vartheta_h,\\ &-\Big(\Upsilon_2(\vartheta_0)\exp(\hat{\boldsymbol{\psi}}_h)-\mathbf{I}\Big):\nabla^s\hat{\boldsymbol{u}}_h\Big],-\rho C_p\hat{\boldsymbol{u}}_h\cdot\nabla\xi_h+k\Delta\xi_h\Big\rangle_K,\end{aligned} \tag{39}$$

The same considerations made for the standard formulation about the projections and the different stabilization methods carry over to the log-conformation reformulation.

### 4.2 Split-OSS stabilization

This stabilization method comes from considering two assumptions in the residual-based VMS methods. The first one is that the projection considered is $\tilde{P}=P_h^{\perp}$, and the second one is to neglect the cross local inner-product terms together with other terms that do not contribute to stability. The result is a simplified method that is not consistent but whose convergence rate in $h$ is optimal, as explained in [29]. The split strategy is only considered over the stabilization terms of the momentum equation, and the reason for this is detailed in [43]. If the split term-by-term in the constitutive equation is done, convergence for the non-linear iterations turns out to be very difficult to attain.

Therefore for the standard formulation, the stabilization considered finally consists in finding $\boldsymbol{U}_h:]0,T[\longrightarrow\boldsymbol{\mathcal{X}}_h$ such that

$$\begin{aligned}&(\mathcal{G}_{\rm std}(\vartheta_h;\boldsymbol{U}_h),\boldsymbol{V}_h)+B_{\rm std}(\boldsymbol{U}_h;\boldsymbol{U}_h,\boldsymbol{V}_h)+S^{\perp}_{1,\rm std}(\boldsymbol{u}_h;\boldsymbol{U}_h,\boldsymbol{V}_h)+S^{\perp}_{2}(\boldsymbol{U}_h,\boldsymbol{V}_h)\\ &\qquad+S^{\perp}_{3,\rm std}(\boldsymbol{U}_h;\boldsymbol{U}_h,\boldsymbol{V}_h)+S^{\perp}_{4,\rm std}(\boldsymbol{u}_h,\boldsymbol{\sigma}_h;\boldsymbol{U}_h,\boldsymbol{V}_h)=L_{\rm std}(\boldsymbol{V}_h).\end{aligned} \tag{40}$$

for all $\boldsymbol{V}_h\in\boldsymbol{\mathcal{X}}_h$. For $S^{\perp}_{i,\rm std}$ with $i=2,3,4$ we consider the same expression detailed in (30), (31) and (32) for $S_{i,\rm std}$, but now taking into account that $\tilde{P}=P_h^{\perp}$ as it has been specified above. The expression of $S^{\perp}_{1,\rm std}$ in (40) is now as follows:

$$\begin{aligned}S^{\perp}_{1,\rm std}\left(\hat{\boldsymbol{u}}_h;\boldsymbol{U}_h,\boldsymbol{V}_h\right)=&\sum_K \alpha_1\left\langle P_h^{\perp}\left[\nabla\cdot\boldsymbol{\sigma}_h\right],\nabla\cdot\boldsymbol{\chi}_h\right\rangle_K+\sum_K \alpha_1\left\langle P_h^{\perp}\left[\nabla p_h\right],q_h\right\rangle_K\\ &+\sum_K \alpha_1\left\langle P_h^{\perp}\left[\nabla\rho\hat{\boldsymbol{u}}_h\cdot\nabla\boldsymbol{u}_h\right],\rho\hat{\boldsymbol{u}}_h\cdot\nabla\boldsymbol{v}_h\right\rangle_K.\end{aligned} \tag{41}$$

For the log-conformation reformulation we have the following stabilized form: find $\boldsymbol{U}_h:]0,T[\longrightarrow\boldsymbol{\mathcal{X}}_h$ such that

$$(\mathcal{G}_{\log}(\vartheta_h;\boldsymbol{U}_h),\boldsymbol{V}_h)+B_{\log}(\boldsymbol{U}_h;\boldsymbol{U}_h,\boldsymbol{V}_h)+S^{\perp}_{1,\log}(\boldsymbol{u}_h,\vartheta_h;\boldsymbol{U}_h,\boldsymbol{V}_h)+S^{\perp}_{2}(\boldsymbol{U}_h,\boldsymbol{V}_h)$$

$$+ S^{\perp}_{3,\log}(\boldsymbol{U}_h;\boldsymbol{U}_h,\boldsymbol{V}_h) + S^{\perp}_{4,\log}(\boldsymbol{U}_h;\boldsymbol{U}_h,\boldsymbol{V}_h) = L_{\log}(\boldsymbol{V}_h), \tag{42}$$

for all $\boldsymbol{V}_h \in \boldsymbol{\mathcal{X}}_h$. As in the standard formulation, for the terms $S^{\perp}_{i,\log}$ with $i = 2, 3, 4$, we can consider the expressions detailed in (36), (37), (39) taking $\tilde{P} = P^{\perp}_h$. The expression of $S^{\perp}_{1,\log}$ in (42) is now as follows:

$$\begin{aligned} S^{\perp}_{1,\log}(\hat{\boldsymbol{u}}_h, \hat{\vartheta}_h;\boldsymbol{U}_h,\boldsymbol{V}_h) = &\sum_K \alpha_1 \Big\langle P^{\perp}_h\Big[\nabla\cdot(\Upsilon_2(\vartheta_0)\exp(\boldsymbol{\psi}_h))\Big], \nabla\cdot\boldsymbol{\chi}_h\Big\rangle_K \\ &+ \sum_K \alpha_1 \Big\langle P^{\perp}_h\Big[\nabla p_h\Big], \nabla q_h\Big\rangle_K + \sum_K \alpha_1 \Big\langle P^{\perp}_h\Big[\rho\hat{\boldsymbol{u}}_h\cdot\nabla\boldsymbol{u}_h\Big], \rho\hat{\boldsymbol{u}}_h\cdot\nabla\boldsymbol{v}_h\Big\rangle_K. \end{aligned}$$

There are many benefits associated to the use a split term-by-term stabilization instead of a residual-based one: the first one is the simplicity, since some cross-local products have been neglected, the second one is that some negative terms that do not contribute to stability have been deleted, therefore the scheme is more stable. Moreover, the scheme has turned out to be more efficient in solving problems with high gradients and when the Weissenberg number is relatively high in viscoelastic fluid flow problems [44, 23]. Furthermore, cumbersome elementwise terms of the form $\nabla\cdot\eta\nabla^s\boldsymbol{v}_h$, with $\eta$ a variable function depending on temperature, do not need to be evaluated.

### 4.3 Linearization and algorithm

The set of equations of the thermally coupled problem with incompressible viscoelastic flows presents a high number of non-linear terms, in particular in the momentum and in the constitutive equation. Regarding the algorithm employed, it is displayed in Algorithm 1 (only considering the standard formulation, however for the log-conformation reformulation the algorithm would be analogous). Let us make the following remarks about the algorithm used:

- It is iterative for the coupling, but monolithic for the fluid flow problem. It means that in each time-step the parameters dependant on temperature for solving the viscoelastic fluid flow problem and the stress work for the temperature problem are continuously updated.
- The nonlinear term in the momentum equation can be linearized with a fixed point scheme or with Newton-Raphson's method.
- In the case of the log-conformation reformulation, the exponential terms that appear both in the momentum equation and in the constitutive equation have been linearized using a Taylor development (see [23]), taking the tensor $\hat{\boldsymbol{\psi}}$ as the one obtained from the previous iteration of the current time step.
- The computation of the exponential function, the gradient and the divergence of the exponential function of the variable $\boldsymbol{\psi}_h$ at the previous iteration must be calculated at each iteration.
- For the convective term of the momentum equation, we can use a fixed point scheme or Newton-Raphson's scheme. However, for the non-linear terms in the constitutive equation, we have used a Newton-Raphson linearization always, and it has been decisive to be able to compute some high Weissenberg number cases and get the optimal convergence of the method.
- Stabilization parameters are computed with the values of the unknowns at the previous iterations.

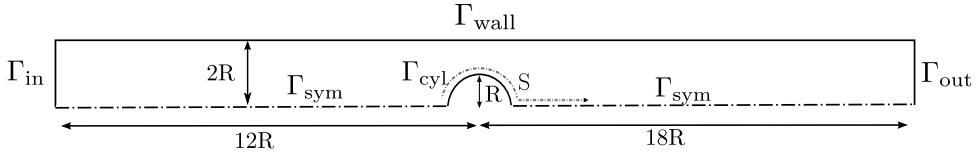


Figure 2: Non-isothermal flow past a cylinder. Geometry and computational boundaries.

- The iterative treatment of the orthogonal projection is coupled to the linearization of the total system. Specifically, the orthogonal projection of any function $f$ has been approximated as $P_h^{\perp}[f^i] \approx f^i - P_h[f^{i-1}]$, the superscript being the iteration counter.

# 5 Numerical results

In this section several numerical examples are presented. Firstly, the flow past a cylinder is studied, using the standard formulation together with the PTT constitutive equation, and taking the Williams-Landel-Ferry function to establish the relations between temperature and viscoelastic parameters. The second example is the extension 1:3, where the log-conformation reformulation is employed, the Oldroyd-B constitutive equation is considered and the Arrhenius function is used, instead of the WLF, as dependence method between temperature and viscoelastic properties. All computations have been performed using the Split-OSS stabilization explained in Section 4.2. Likewise, for each case the formulation chosen corresponds to that of the reference of comparison, when possible.

## 5.1 Flow around a cylinder

The first example is the well-known flow past a cylinder, a typical benchmark to check formulations for simulating viscoelastic fluid flows. This has been extensively studied by Peters and Baaijens [45] to evaluate the performance of constitutive equations for both polymer solutions and melts, although supposing an isothermal flow. Moreover, these authors also explore the non-isothermal case in [2]. There, the numerical result is obtained using a stabilized discontinuous Galerkin method for the viscoelastic equations, and a regular Galerkin method employing a bi-quadratic interpolation of the temperature to solve the temperature equation. Coupling is carried out using a fixed point iteration. The authors also discuss the differences in the stress field between isothermal and non-isothermal problems, as we will do.

### 5.1.1 Setup

The computational domain extends 12 times the length of the radius upstream of the cylinder centre and 18 times downstream, as shown in Figure 2.

First, we define the parameters of the non-isothermal viscoelastic fluid flow problem. The relaxation time for the reference temperature $\lambda(\vartheta_0)$ is 0.1 s, the total viscosity for the reference temperature is $\eta_0(\vartheta_0) = 1.0 \times 10^4$ Pa $\cdot$ s, and the parameter $\beta$ is set to 0.5. As it has been explained, the total viscosity and relaxation time are temperature-dependent, and this relation is defined by the WLF function $g_{\text{wlf}}$ defined in Section 2.1. In this case the constants $c_1$ and $c_2$ of this function are set as 4.54 and 150.36, respectively. The mobility parameter $\varepsilon$ of the PTT constitutive model is 0.1. The density is $\rho = 921$ kg $\cdot$ m$^{-3}$, the specific heat is $C_p = 1.5$ kJ $\cdot$ kg $\cdot$ K$^{-1}$ and the conductivity $k$ is fixed to 0.17 W $\cdot$ m $\cdot$ K$^{-1}$. The reference temperature $\vartheta_0$ is set to 462 K.

**Algorithm 1** General algorithm for thermal coupling using VMS.

**read** initial condition $\boldsymbol{u}_h^0$ and $\vartheta_h^0$
**set** $p_h^0 = 0$, $\boldsymbol{\psi}_h^0 = \mathbf{0}$
**for** $j = 0, ..., m-1$ **do** *(Temporal loop)*
  **set** $k$=0
  **set** $\boldsymbol{u}_h^{j+1,0} = \boldsymbol{u}_h^j$, $p_h^{j+1,0} = p_h^j$, $\boldsymbol{\sigma}_h^{j+1,0} = \boldsymbol{\sigma}_h^j$
  **while** not converged **do** *(Coupling loop)*
    $k \leftarrow k+1$
    **set** $i = 0$
    **set** $\boldsymbol{u}_h^{j+1,k,0} = \boldsymbol{u}_h^{j,k}$, $p_h^{j+1,k,0} = p_h^{j,k}$, $\boldsymbol{\sigma}_h^{j+1,k,0} = \boldsymbol{\sigma}_h^{j,k}$
    **set** $\lambda^{j+1,k} = \lambda(\vartheta_h^{j+1,k-1})$ and $\eta_0^{j+1,k} = \eta_0(\vartheta_h^{j+1,k-1})$
    **while** not converged **do**
      $i \leftarrow i+1$
      **compute** "residuals": $\mathbf{R}_{u1}$, $\mathbf{R}_{u2}$, $\mathbf{R}_{u3}$, $\mathbf{R}_\sigma$
      **compute** projections: $P_h[\mathbf{R}_{u1}]$, $P_h[\mathbf{R}_{u2}]$, $P_h[\mathbf{R}_{u3}]$, $P_h[\mathbf{R}_\sigma]$
      **compute** stabilization parameters:
        $\alpha_1^{j+1,k,i-1}$, $\alpha_2^{j+1,k,i-1}$ and $\alpha_3^{j+1,k,i-1}$ with $\boldsymbol{U}^{j+1,k,i-1}$
      **solve** viscoelastic fluid flow equations for $\boldsymbol{u}_h^{j+1,k,i}$, $p_h^{j+1,k,i}$ and $\boldsymbol{\sigma}_h^{j+1,k,i}$
      **check** convergence
    **end while**
    **set** converged values
      $\boldsymbol{u}_h^{j+1,k} = \boldsymbol{u}_h^{j+1,k,i}$
      $p_h^{j+1,k} = p_h^{j+1,k,i}$
      $\boldsymbol{\sigma}_h^{j+1,k} = \boldsymbol{\sigma}_h^{j+1,k,i}$
    **set** the stress work as $\boldsymbol{\sigma}_h^{j+1,k} : \nabla \boldsymbol{u}_h^{j+1,k}$
    **set** $i = 0$
    **set** $\vartheta_h^{j+1,k,0} = \vartheta_h^{j,k}$
    **compute** stabilization parameter $\alpha_4^{j+1,k,i-1}$ with $\boldsymbol{u}_h^{j+1,k}$
    **while** not converged **do**
      $i \leftarrow i+1$
      **compute** "residual" $\mathbf{R}_\vartheta$
      **compute** projection $P_h[\mathbf{R}_\vartheta]$
      **solve** the energy equation for $\vartheta_h^{j+1,k,i}$ considering the stress work
      **check** convergence
    **end while**
    **set** converged values
      $\vartheta_h^{j+1,k} = \vartheta_h^{j+1,k,i}$
  **end while***(End coupling loop)*
  **set** converged values
    $\boldsymbol{u}_h^{j+1} = \boldsymbol{u}_h^{j+1,k}$
    $p_h^{j+1} = p_h^{j+1,k}$
    $\boldsymbol{\sigma}_h^{j+1} = \boldsymbol{\sigma}_h^{j+1,k}$
    $\vartheta_h^{j+1} = \vartheta_h^{j+1,k}$
**end for***(End temporal loop)*

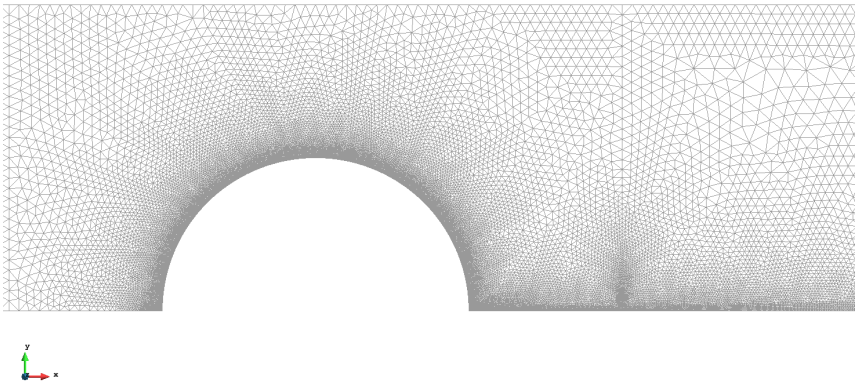

Figure 3: Non-isothermal flow past a cylinder. Zoom of computational mesh employed.

Regarding the boundary conditions of the problem, for the velocity no-slip conditions are imposed on the top wall $\Gamma_{\text{wall}}$ and the cylinder surface $\Gamma_{\text{cyl}}$, and symmetry conditions are prescribed along the axis $\Gamma_{\text{sym}}$. On the other hand, a fully developed parabolic velocity profile and the associated elastic stress are prescribed at the inlet $\Gamma_{\text{in}}$. These are given by:

$$u_x = \frac{3Q}{8\text{R}}\left(1 - \frac{y^2}{(2\text{R})^2}\right), \qquad u_y = 0,$$

$$\sigma_{xx} = 2\lambda(\vartheta_0)(1-\beta)\eta_0(\vartheta_0)\left(\frac{\partial u_x}{\partial y}\right)^2, \qquad \sigma_{xy} = (1-\beta)\eta_0(\vartheta_0)\left(\frac{\partial u_x}{\partial y}\right), \qquad \sigma_{yy} = 0,$$

where $Q$ is the flow rate, and R is the cylinder radius. Note that stresses are prescribed using the Oldroyd-B model and with the only purpose of accelerating convergence. For the outlet $\Gamma_{\text{out}}$, the horizontal velocity is left free, the vertical velocity is taken equal to zero and the pressure is prescribed to zero. On the other hand, regarding the temperature boundary conditions, the reference temperature $\vartheta_0$ is imposed at the inlet $\Gamma_{\text{in}}$ and on the top wall $\Gamma_{\text{wall}}$ as 462 K.

We will compute the problem for different Weissenberg numbers (already defined in Section 2.2) We $= \lambda U/R$ where $U$ is the characteristic velocity, written as a function of the flow rate as $U = 3Q/2\text{R}$; R is the cylinder radius defined above. As considered in reference [2], the convective term of the momentum equation is neglected in all the computations.

About the FE discretization considered, the mesh has 58591 linear elements and 36174 nodes. We have to remark that the refinement around the cylinder wall is significant, as shown in Figure 3, where the mesh is partially shown. Although all simulations have a steady-state solution, all of them have been computed using a temporal discretization to facilitate the convergence of the iterative algorithm. For all the cases, the scheme used is BDF1 (as explained in Section 3), and the time step is fixed to $\delta t = 5 \times 10^{-5}$ s.

### 5.1.2 Results

Results of the simulation for We $= 4.0$ are shown in Figures 4 and 5. In particular, Figure 4 shows the distribution of the temperature in the vicinity of the cylinder while Figure 5 displays the distribution of the stresses in the same location.

- For the distribution of the temperature, this field rises significantly downstream, reaching the maximum temperature at 474.42 K. The difference of temperature between the initial or the temperature fixed on the walls at 462 K and the maximum temperature reached is the consequence of the stress work, represented by the term added to the energy equation, expressed as the product between the stresses and

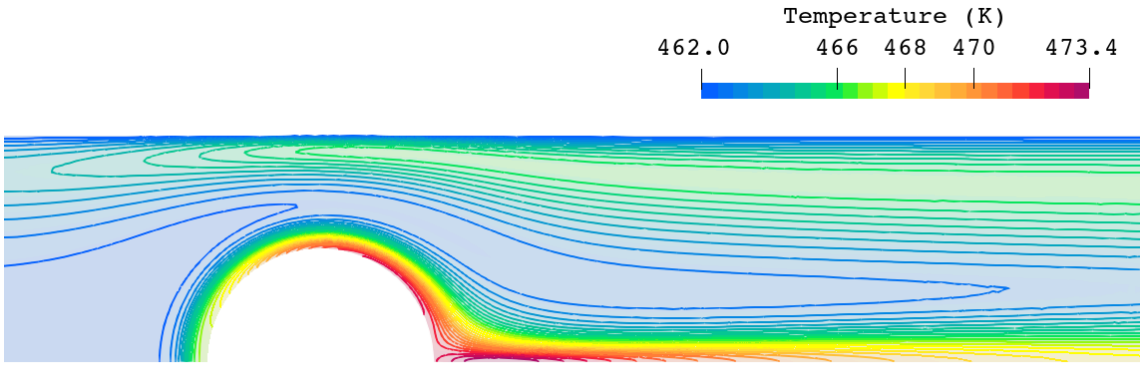


Figure 4: Non-isothermal flow past a cylinder. Distribution of temperature $\vartheta$ around the cylinder. We = 4.

the symmetric gradient of the velocity field. In comparison with the typical models associated with Newtonian fluid flows, the viscoelastic fluid flow has a new *source* of heat, which is represented in the Figure 4. On the other hand, in comparison with [2], the maximum value reached is slightly smaller, although the general distribution of the temperature field is similar to the one obtained by the authors of this reference.

- Regarding the distribution of the stresses in Figure 5 near the cylinder, the maximum values are reached in two significant locations: one in the top of the wall of the cylinder, and another one at a point downstream, located in the centerline (or symmetric boundary) of the domain.

The temperature effect over the stress field can be shown in Figure 6, where the isothermal case is compared with the non-isothermal case, and both cases considering We = 4.0. As this figure shows, a significant reduction in stresses is found when the temperature coupling is considered. That reduction is located both over the wall of the cylinder and downstream. In [2], the reduction reached in the stresses is over 40% comparing two cases. Although in our computations this difference is not so pronounced as in the reference work, the reduction is equally considerable, over the 30%.

In Figure 7, a comparison between the difference of temperatures is performed between the viscoelastic case for We = 4 and the Newtonian viscous case. At first sight, the major difference is that the viscoelastic case reaches higher temperatures than the Newtonian case; however, the temperature distribution on the cylinder and downstream is also significantly different. While in the viscoelastic case the maximum peak of temperature is reached downstream, in the Newtonian case it is reached on the cylinder. On the other hand, computations were executed for some Weissenberg numbers to study the differences between temperatures. The parameter $\Delta\vartheta = \vartheta - \vartheta_0$ (difference between reference temperature and temperature distribution), around the cylinder is plotted in Figure 8. The results in these last figures seem to be coherent: while the Weissenberg number increases, the stresses also do, and therefore by the definition of viscous dissipation the internal work is more relevant, causing an increase of the temperature around the cylinder and downstream. Results are in agreement with the graph shown in [2] from a qualitative point of view. Quantitatively, the comparison is not meaningful, as we have not performed mesh convergence studies and these are not presented in [2], either.

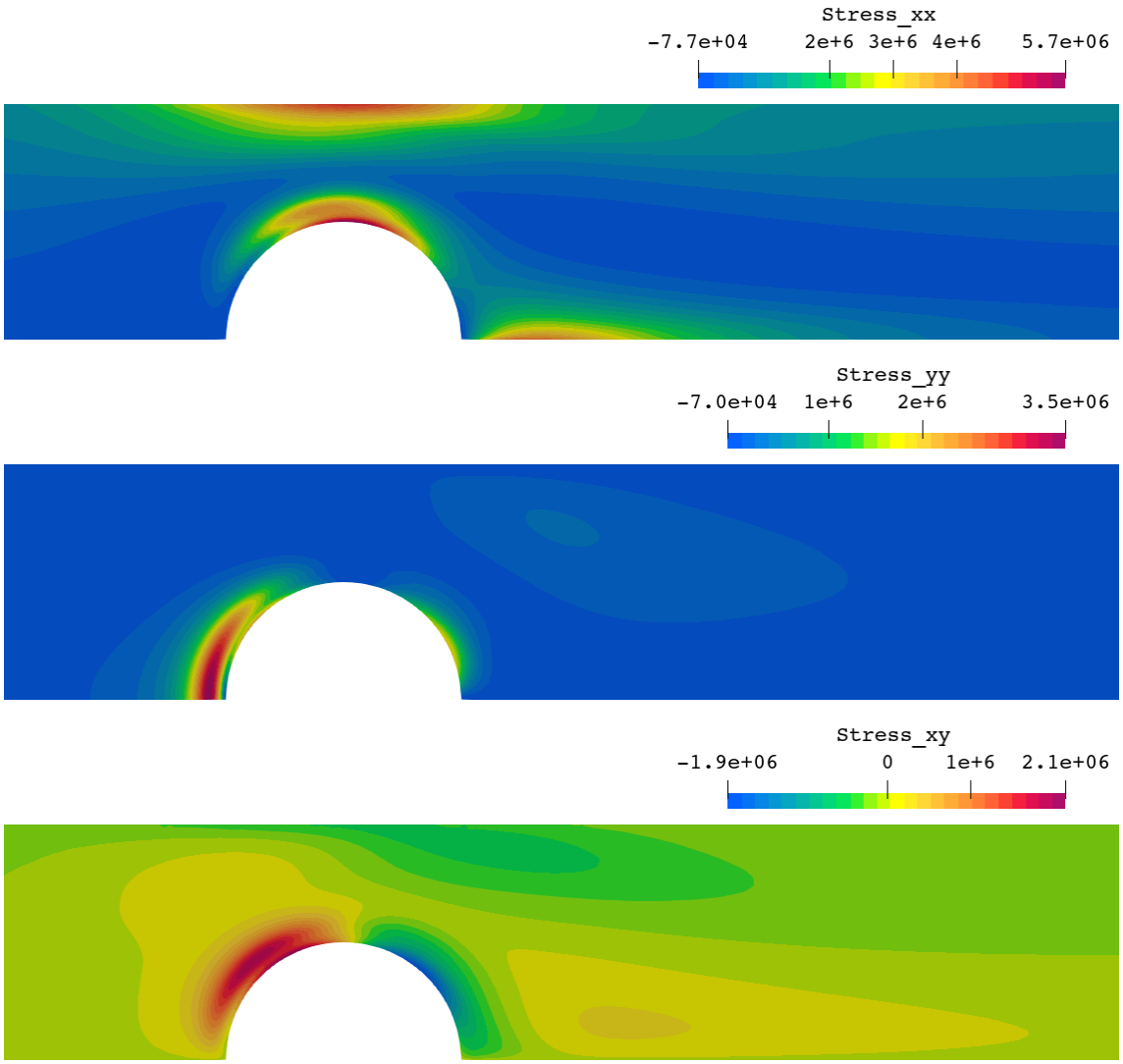


Figure 5: Non-isothermal flow past a cylinder. Distribution of stresses. Above: component $\sigma_{xx}$, middle: component $\sigma_{yy}$ , and below: component $\sigma_{xy}$ around the cylinder. We = 4.

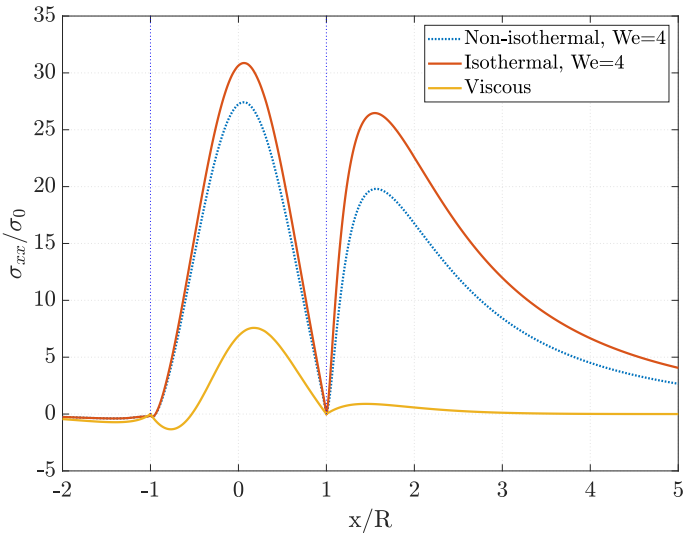


Figure 6: Non-isothermal past flow a cylinder. Stress component $\sigma_{xx}$ around and downstream of cylinder in isothermal and non-isothermal cases.

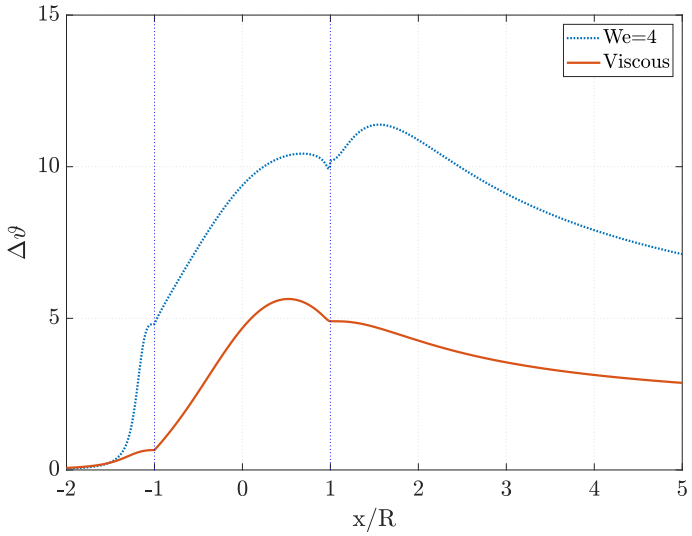


Figure 7: Non-isothermal flow past a cylinder. Increase of temperatures around the cylinder and downstream for Newtonian fluid and a viscoelastic fluid, We = 4.

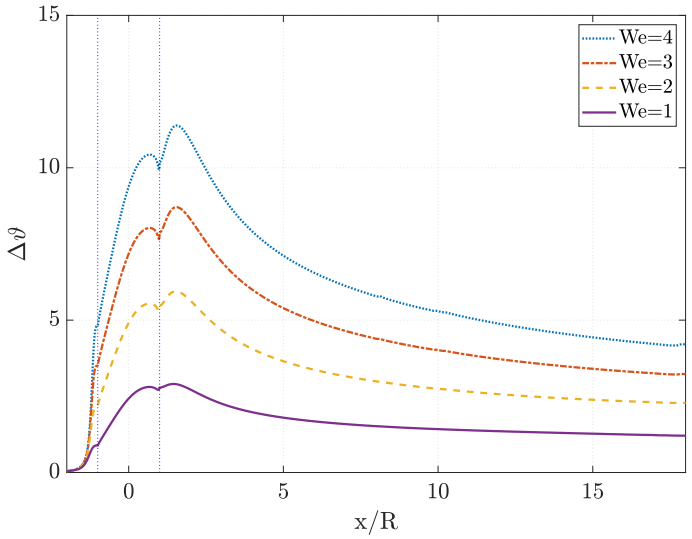


Figure 8: Non-isothermal flow past a cylinder. Increase of temperatures around the cylinder and downstream for several Weissenberg numbers.

### 5.2 1:3 Expansion

In this section, the case of the 1:3 expansion is simulated. This benchmark is motivated by the work of Shahbani-Zahiri et al. [11], where a complete study is done of this problem, exploring the solution for different expansion angles. That is an important example due to the formation and growth of symmetric and asymmetric regions that play an important role in the viscous dissipation, temperature distribution, and heat transfer rate. Following ideas similar to those exposed in the cited paper, we study the temperature effect over the patterns. On the one hand, both the fluid inertia and elasticity have a significant effect on the flow pattern of non-isothermal viscoelastic fluids, and therefore, the research of the effects of elastic properties and inertial force on the heat transfer is relevant and worth. In the literature, more papers treat this problem for a low Reynolds (when bifurcation effects are not present) than for a relatively high Reynolds number. When the Reynolds number is around 50 or 100 the flow of Newtonian fluids is known to give rise to an asymmetric pattern: larger and smaller recirculation zones appear behind the step change. This phenomenon is characteristic in planar expansions, and it is suggested in [46] that this could be explained by the Coanda effect. This effect explains that any perturbation of the flow field, pushing the main flow to one of the sides of the expansion, gives rise to larger velocities and lower pressures. Consequently, the asymmetry will naturally tend to be accentuated. This example has an additional peculiarity: the asymmetry of the steady-state solution if the Reynolds number is greater or equal than 40 or/and if the Elasticity number El= We/Re is greater than 0.1, even if the geometry is symmetrical. This asymmetry was accurately studied in the literature, under theoretical, experimental, and numerical works with Newtonian fluids, such as [47], [48], or the work developed by Hawa et al. [49], where a bifurcation analysis and linear stability study is carried out. Additionally we have to remark the works [50] and [46]. In [46], Oliveira studies the bifurcation in different isothermal scenarios that include Newtonian and viscoelastic fluid flows, simulating the problem with a finite volume method for a FENE type constitutive model.

In [11] the constitutive model employed is the so called exponential Phan Thien-Tanner (EPTT) model, similar to the PTT model explained in this paper, with the difference that the exponential of $\mathfrak{h}(\boldsymbol{\sigma})$ is considered, using the notation introduced in Section 2.1. In our computations, the Oldroyd-B constitutive model is employed, but instead of the standard formulation, the log-conformation approach is used. This formulation seems to be more adequate than the standard one due to the high Weissenberg number reached in some computations.

In this section, apart from studying the thermal coupling, we will explore also the effect of the four dimensionless numbers that characterize the problem; how the flow pattern, and the temperature distribution change as the Weissenberg number (elasticity) increases or the Prandtl and the Brinkman number vary. Note that in the reference work [11] only the inertial and the elasticity influence are reported.

#### 5.2.1 Setup

The computational geometry for this problem is represented in Figure 9a. In this case, the parameters of the model are as follows: h = 0.1 m (not to be confused with the mesh size), H = 0.3 m, $\theta = 60°$. Regarding the lengths of the three parts of the duct, these are set as: $L_1 = 60$h m, $L_3 = 120$h m and $L_2$ is calculated taking into account the angle of the expansion, therefore it is set as $L_2 = \frac{1}{5\sqrt{3}}$ m. Regarding the computational mesh, different grids have been employed for the computations, but all of them considering Q1 (bilinear) elements, following the structure displayed in Figure 9b. The characteristics of the mesh are detailed in Table 1 where NY indicates the number of the mesh cells in the

| Mesh | NY | $\Delta y_{\min}$ | NX1 | NX2 | $\Delta x_{\min}$ | Nodes | Elements |
|---|---|---|---|---|---|---|---|
| M1 | 20 | 0.0050 | 140 | 400 | 0.0072 | 11 781 | 11 200 |
| M3 | 52 | 0.0019 | 358 | 1024 | 0.0027 | 72 384 | 73 829 |

Table 1: 1:3 expansion. Main characteristics of the meshes employed.

$y$-direction of the channel. Moreover, NX1 and NX2 are the number of mesh cells for the first and second sections of the channel in the $x$-direction.

The Reynolds number can be computed using the maximum inlet velocity (from this point it will be indicated as $\mathrm{Re}_{\max} = \rho U_{\max} L/\eta_0$) or using the average of the incoming velocity (denoted by $\mathrm{Re}_{\mathrm{avg}} = \rho U_{\mathrm{avg}} L/\eta_0$ to avoid future confusions). The characteristic length is taken as h (height of the small channel). The remaining fluid parameters are: $\eta_0 = 4.07$ Pa $\cdot$ s, $\rho = 1226$ kg$\cdot$m$^{-3}$, and $\beta = 0.5$ (recall that $\eta_s = \beta\eta_0$, $\eta_p = (1-\beta)\eta_0$). For the Arrhenius function, the constant $c_r$ is 1720 K. Regarding the temperature parameters, these are the specific heat $C_p$ and conductivity $k$, computed using the Brinkman number and the Prandt number, which are suitably defined at the end of Section 2.2. The reference temperature $\vartheta_0$ is set to 463.5 K. Now we define the boundary conditions. For the velocity, no-slip conditions are imposed on the walls of the channel $\Gamma_{\mathrm{wall}}$ and a fully developed parabolic velocity profile together with the associated elastic stress are prescribed at the inlet $\Gamma_{\mathrm{in}}$. These are given by:

$$u_x = \frac{3Q}{4\mathrm{h}}\left(1 - \frac{y^2}{\mathrm{h}^2}\right), \qquad u_y = 0,$$

$$\sigma_{xx} = 2\lambda(\vartheta_0)(1-\beta)\eta_0(\vartheta_0)\left(\frac{\partial u_x}{\partial y}\right)^2, \qquad \sigma_{xy} = (1-\beta)\eta_0(\vartheta_0)\left(\frac{\partial u_x}{\partial u_y}\right), \qquad \sigma_{yy} = 0,$$

where $Q$ is the flow rate, and $h$ is the height of the small channel. For the outlet $\Gamma_{\mathrm{out}}$, the horizontal velocity is left free, the vertical velocity is taken equal to zero and the pressure is prescribed to zero, constant. On the other hand, regarding the temperature boundary conditions, the reference temperature $\vartheta_0$ is imposed at the inlet $\Gamma_{\mathrm{in}}$ and on the top wall $\Gamma_{\mathrm{wall}}$ to 563.15 K. Note that the inlet fluid is 100 K colder than the temperature of the walls.

### 5.2.2 Newtonian case. Validation

The Newtonian case is computed for the isothermal case first for validations, as this case is widely reported in the literature. Later the results will be compared with the thermally-coupled case. Very similar results are obtained for meshes M1 and M3, showing that the results obtained can be used for comparison with the literature. In particular, this comparison is done using the results of mesh M3, although mesh M1 is employed to study the trend of the vortices when different dimensionless numbers are changed.

As it is explained in [46], in most earlier calculations of the phenomenon, the asymmetric flow was usually triggered by introducing a slight geometrical asymmetry in the symmetric configuration or by adding a small perturbation to the velocity profile imposed at the inlet or to the whole initial velocity field (see, for example, [51, 47, 48, 49, 52]). In our case, as happened in the work of Oliveira et al. [46], no artificial devices have been required if the ASGS stabilization is employed. However, if the stabilization is of split-type and the Reynolds number is low, the bifurcation must be triggered using a bifurcation produced by a higher Reynolds number as an initial solution, for example. In the case of Newtonian fluid considering the isothermal case, the critical Reynolds number at which bifurcation occurs found for our computations is $\mathrm{Re}_{\mathrm{c}} = 53.5$. Comparing with the

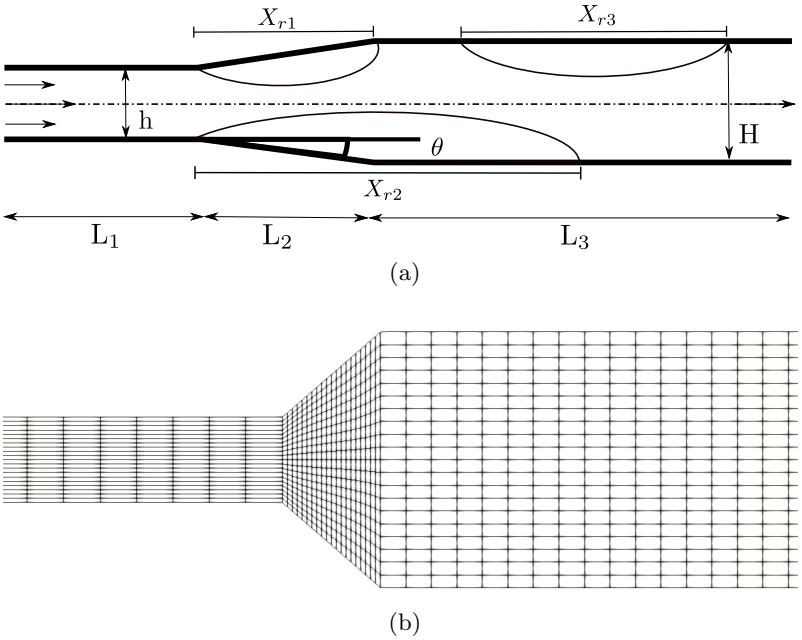


Figure 9: 1:3 expansion. Computational geometry and scheme of vortices (a) and computational mesh M1 (b).

| **Authors** | **Critical Reynolds** |
|---|---|
| Oliveira et. al [46] | 54.0 |
| Fearn et al. [47] | 53.9 |
| Drikakis et al. [48] | 53.3 |
| Hawa and Rusak [49] | 53.8 |
| Mishra and Jayaraman [51] | 53.0 |
| Present Study | 53.5 |

Table 2: 1:3 expansion. Comparison of critical Reynolds in literature for the pitchfork bifurcation.

literature, this approach is rather accurate, considering that different methods have been applied in each case. For example, in the work of Oliveira et al. [46] the critical value is $\mathrm{Re_c} = 54$ using a finite volume method; for Fearn et al. [47] it was $\mathrm{Re_c} = 53.9$ using in that case a FE framework. We can find also the work of Drikakis [48] which uses a fourth-order finite-difference method and the critical Reynolds value is $\mathrm{Re_c} = 53.3$. In the literature, we find also other examples such as the work of Hawa and Rusak [49], which employ a stream function finite-difference formulation and where the critical Reynolds number is $\mathrm{Re_c} = 53.8$. In Table 2, this comparison is summarized. The goal of this study is not to be accurate in the exact location of this critical number, but to validate the algorithm and check the thermal coupling for considering later the viscoelastic case from a qualitative point of view.

For the coupling with the temperature, we consider a Weissenberg number equal to zero to study the differences with the isothermal case. On the other hand, we fix the Prandtl number to 1 and the Brinkman number also to 1. The Reynolds and the Weissenberg numbers are computed taking the average of the fluid velocity at the channel inlet. The parameters of the problem are determined according to the values of these dimensionless numbers.

In Figures 10 and 11 several plots of the stationary solution have been taken for differ-

ent Reynolds numbers to show some aspects of this problem: the streamlines in each case and the distribution of the temperatures. All the plots correspond to the non-isothermal Newtonian case, although the pattern of vortices is similar in all the computation cases. These plots include from relatively low Reynolds number such as Re = 10, where a symmetric solution with small vortices is shown, up to Re = 200, when the stationary solution presents additional vortices.

- It can be observed in Figure 10 that for Re = 10 and Re = 30 the solution is symmetric, although we can see as the length of the vortices is higher as the Reynolds number increases. For Re = 50 the solution has bifurcated and presents an asymmetry: now the vortex on the top is smaller than the vortex in the bottom. Finally, for Re = 100 we can see that apart from the non-symmetric solution, a new vortex has emerged on the top, although displaced downstream. In other words, when the inertial forces are more dominant in comparison with the viscous forces, the fluid flow becomes unstable and the asymmetry appears.

- Regarding the contours of temperature, we can see graphically the effect of the viscous dissipation. As it was specified in the Setup section of the problem, the temperature at the inlet of the channel is 100 K lower than on the walls. Despite this fact, viscous dissipation generates energy in the flowing fluid, reaching the maximum peak when the fluid flow does the transition from the small part of the channel to the wider part. This effect is due to the formation of symmetric recirculation regions, causing a displacement of the maximum peak of heat in the central zone. Moreover, we have to stand out that the maximum value of temperature is moved into the channel when the Reynolds number increases. When Re grows and there is a formation of asymmetric vortices, the location of the maximum temperature zone slightly diverges to the wall where the smaller vortices are formed. Therefore, the maximum temperature zone is generated in the vicinity of the largest vortex and close to its center. These results are in agreement with the results reported by Shahbani-Zahiri [11].

In Figure 11 we plot also streamlines and temperature contours for a higher Reynolds number.

- For Re = 150 we can remark that the vortices have been enlarged in comparison with the case Re = 100, and how the vortex on the top starts to split into two separated vortices. For Re = 200, the plot of streamlines shows the appearance of a new vortex near the bottom wall, apart from the evident enlargement of some of the other vortices.

- The distribution of temperature displays a pronounced gradient of temperatures, and note that the small channel transports a cold flux. In this case, it seems clear that the advection velocity in the energy equation has an important role in this change of temperature distribution. Even the maximum peak of temperatures is not located now at the center of the channel, it can be found in one of the asymmetric vortices.

Now, we will compare the length of the vortices between different cases (isothermal and non-isothermal). Note that in Figure 9a a general scheme of the vortices is plotted in the domain, apart from the general notation to describe this domain. This comparison is displayed in Figure 12, considering both cases: the isothermal (plotted in blue) and the non-isothermal (plotted in red) cases for the Newtonian fluid flow.

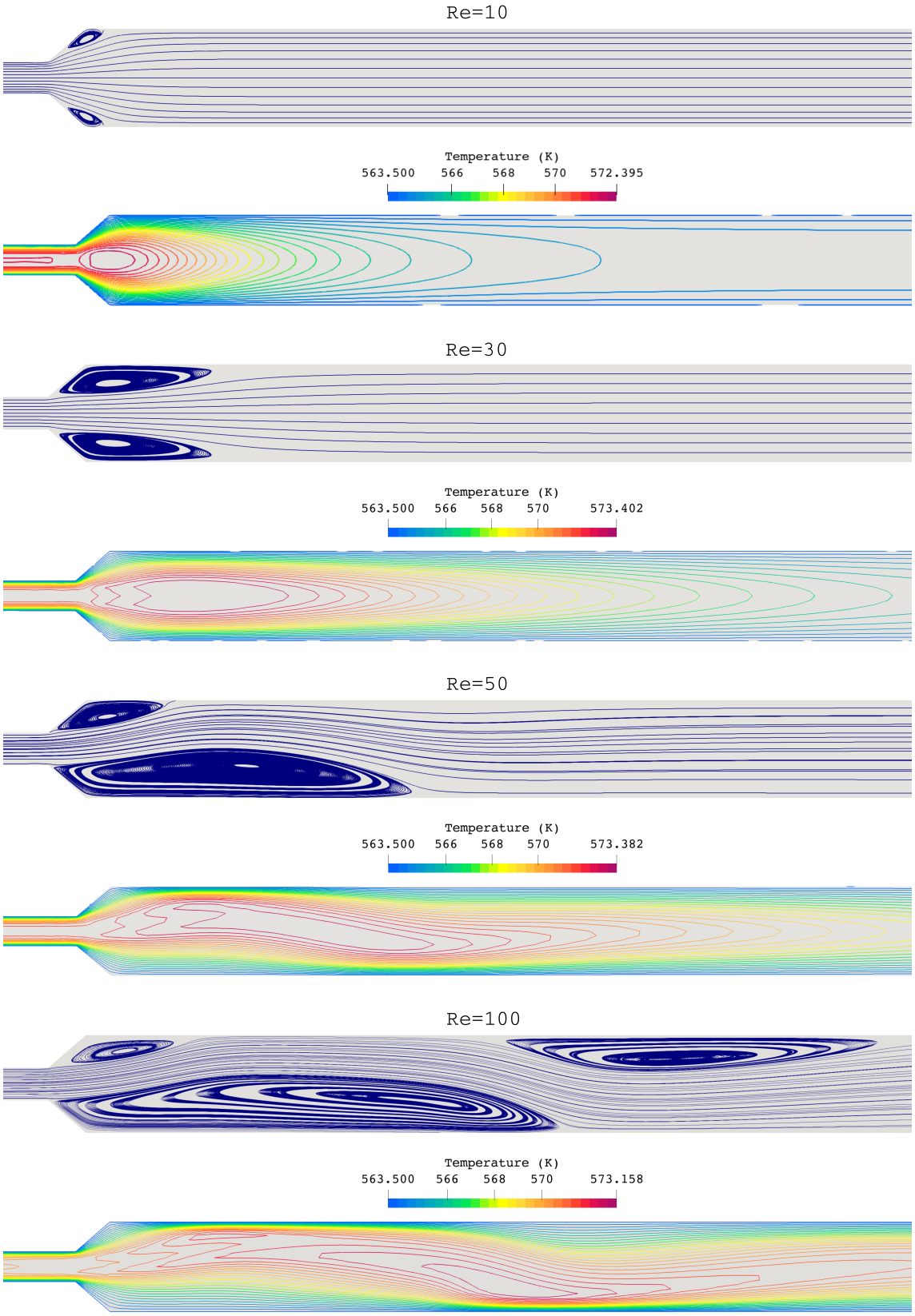


Figure 10: Streamlines and temperature contours for Re = 10, 30, 50 and 100.

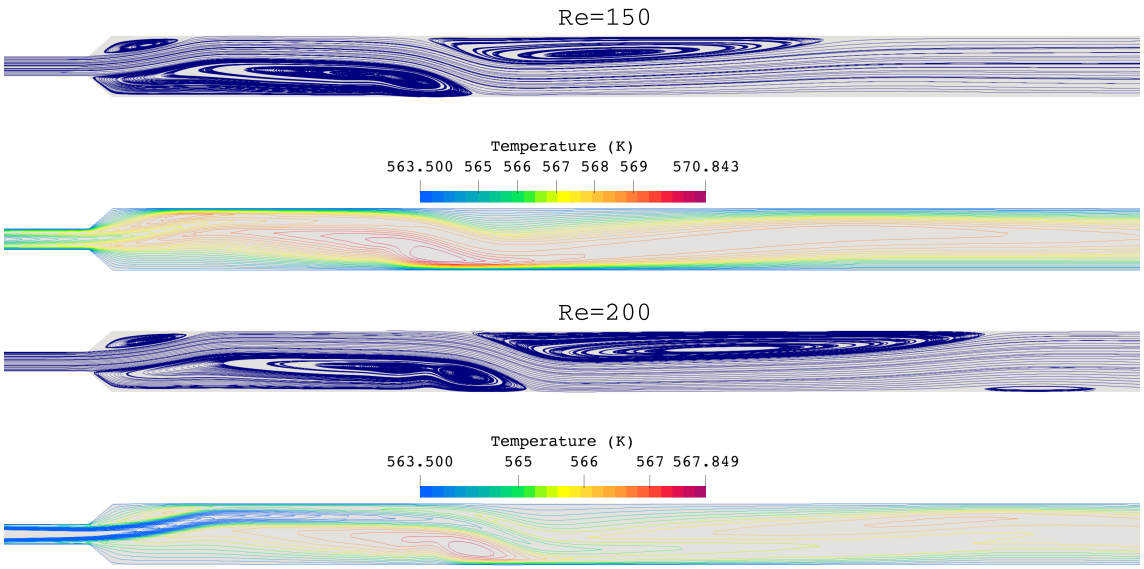


Figure 11: 1:3 expansion. Streamlines and temperature contours for Re = 150 and Re = 200.

- At the first sight, the length of the vortices in the non-isothermal case is higher than in the isothermal scenario, but that is not the only difference, also the critical Reynolds number where the bifurcation occurs has changed significantly. As we have analyzed previously, while the first bifurcation occurs for a critical Reynolds around 53-54 for the isothermal case, if the thermal coupling is considered, that first bifurcation is found around a $\mathrm{Re_c} = 30$.
- The difference between Reynolds numbers is even more pronounced for the second bifurcation: while in the isothermal case the critical Reynolds is 117 (from this point a third vortex emerges in the same side of the channel than the smaller vortex, as represented in Figure 9a), in the non-isothermal case the critical number is around 60. In this last case, the third vortex grows significantly, even overtaking in length vortex $X_{r1}$ (that occurs for Re = 150, for example).

### 5.2.3 Weissenberg number study

As it was commented previously, for non-Newtonian viscoelastic flows the number of independent parameters that can be varied increments significantly. We can now modify the Weissenberg number or the $\beta$ (that measures the balance between polymeric and solvent viscosity) parameters, for example, apart from the Reynolds number. We have to remark that the log-conformation reformulation to solve the problem in the case of high Weissenberg numbers has been crucial to obtaining solutions, despite the increment of the computational cost associated with that formulation [23].

In this study, the main results will put the focus on how viscoelasticity influences the variation of upper and lower vortices in the example we are analyzing. In this sense, we can observe the plots in Figure 13, where a comparison of the length of vortices for varying Reynolds numbers is displayed. The bifurcation plot for the viscoelastic liquid for different Weissenberg numbers is compared with that of the Newtonian case. As it is concluded in Oliveira et al. [46], two main conclusions can be drawn:

- The first one is the fact that the critical Reynolds number in which the bifurcation (transition between symmetric and asymmetric solution) is produced is delayed to

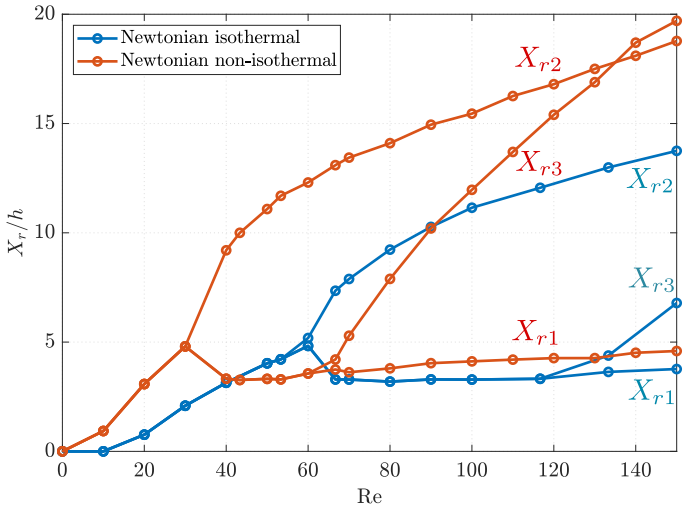


Figure 12: 1:3 expansion. Length of vortices versus the Reynolds number for the Newtonian fluid flow.

higher values. For the Newtonian case, that number is around 53.3, and in our computations, for We = 1 it is around 60, and for We = 2 the critical number is around 67. Therefore, we can conclude that viscoelasticity is a stabilizing factor, retarding the appearance of the asymmetric solution with respect to the We number. In terms of the elastic forces, we can conclude that when these are more relevant in relation with viscous forces, then the fluid flow is more stable.

- The second one is the size of the vortices. In general, for viscoelastic cases, the size is smaller when it is compared with the Newtonian case (see Figure 13a), in particular for the higher vortex $X_{r1}$. For the smaller vortex, a contrary effect occurs: the size is higher. Therefore, we can conclude that the difference between vortices is lower in the presence of elasticity. That occurs clearly in a Reynolds number range between 0 and 100; when the Reynolds number is more relevant, the effect of viscoelasticity is not that remarkable in this aspect.

- In Figure 13b we compare the size of the vortices with the Weissenberg number, with a range of We from 0 to 2. This plot reinforces the previous idea: that elasticity is a stabilizing factor of the bifurcation. The difference between vortices is smaller (the smaller vortex increases while the larger vortex decreases) when the Weissenberg number increases, until the symmetry of the solution is recovered for a We = 2.

In Figure 14, the effect of temperature is analyzed in the viscoelastic case, in particular taking We = 1. A similar effect as the one reported in the Newtonian case is reproduced here: an increase of vortex length and the asymmetry appearing at a low Reynolds number for the non-isothermal case. Also, a comparison between non-isothermal cases considering different Weissenberg numbers (We = 1, 2, 3) together with the Newtonian case was carried out; however, no significant differences were found referring to the vortex length or the Reynolds number where the asymmetry occurs. The reason seems to be that the length of the vortices is dominated mainly by the Prandtl number when the coupling is considered.

Despite the length of the vortex not being affected by elasticity, in Figure 15 the maximum temperature peaks are plotted in both cases: the Newtonian one and the viscoelastic case considering We = 1. As in the previous benchmark, an increase of temperature is noticed when the viscoelastic fluid flow is contemplated.

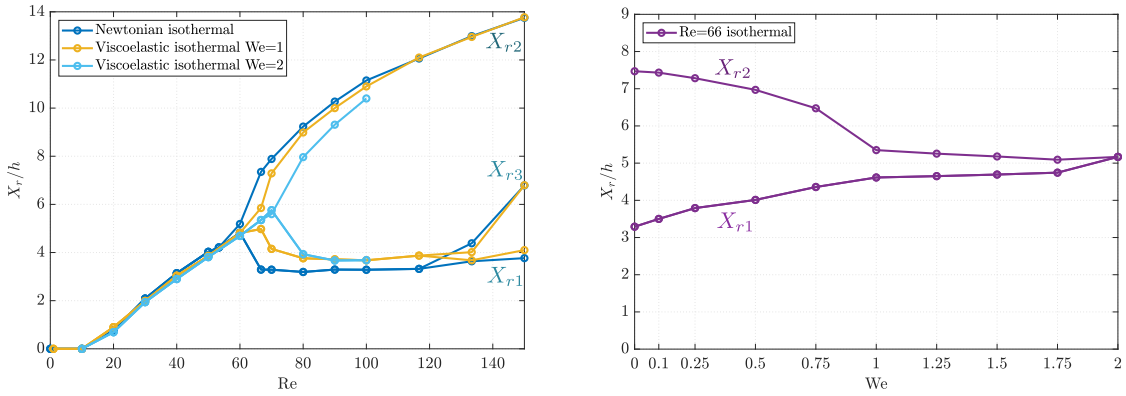


Figure 13: 1:3 expansion. Length of vortices versus the Reynolds number (a), and length of vortices versus the Weissenberg number for Re = 66.67 (b).

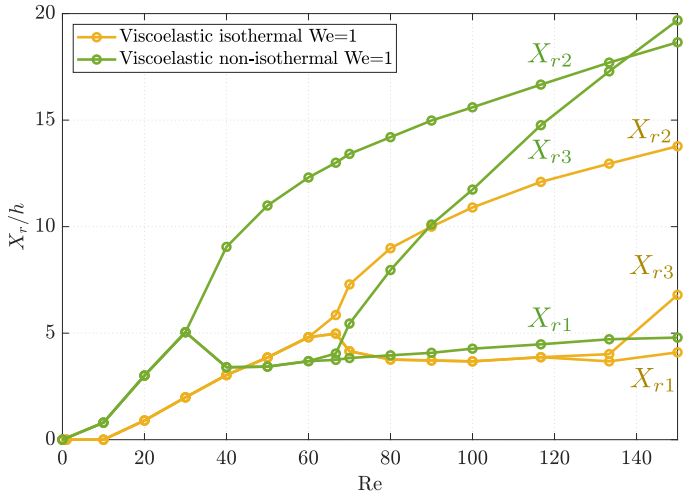


Figure 14: 1:3 expansion. Viscoelastic fluid flow considering the coupling for temperature with Pr = 1, Br = 1.

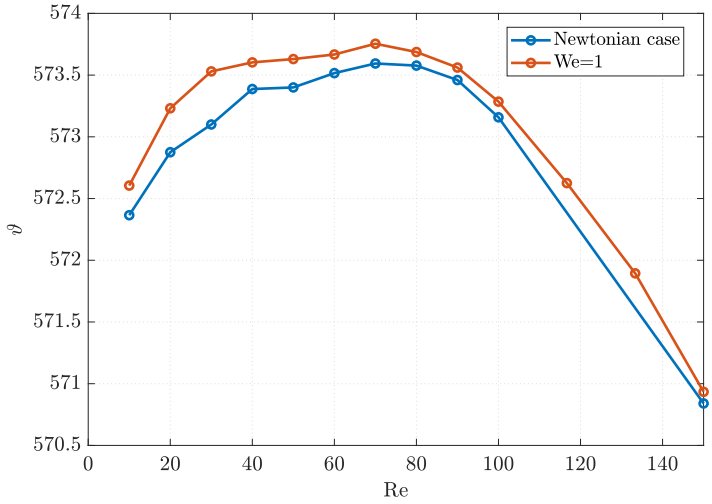


Figure 15: 1:3 expansion. Maximum peaks of temperatures with Pr = 1, Br = 1.

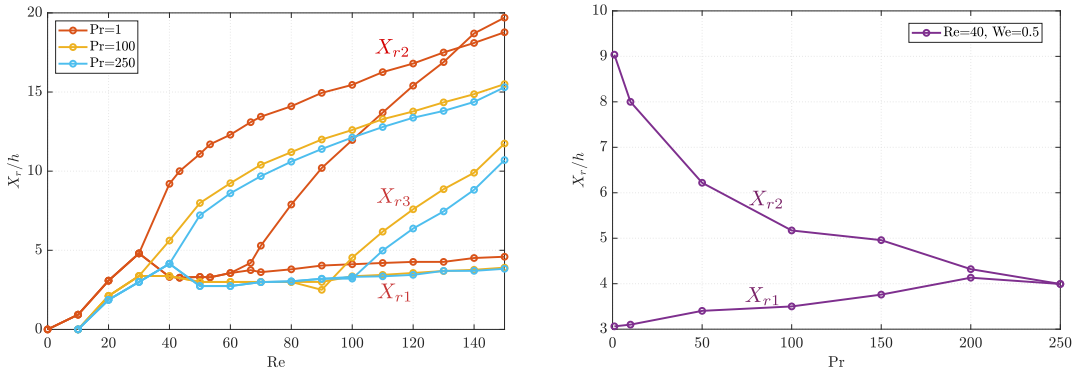


(a) (b)

Figure 16: 1:3 expansion. Effect of Prandtl number on vortex length, We = 0.1, Br = 1. Length of vortices versus the Reynolds number (a), and length of vortices versus the Prandtl number for Re = 40 (b).

### 5.2.4 Prandtl number study

The influence of the Prandtl number on the temperature and on the vortices length is investigated to see how the flow pattern changes when it is increased. In Figure 16 we can observe with more detail that effect.

- Firstly, in Figure 16a we compare the vortices for three different Prandtl number, varying the Reynolds number. Apart from the fact that the vortices are smaller in general when the Prandtl number is greater, also the critical Reynolds where the bifurcation occurs changes. While for Pr = 1 and Pr = 100 the first bifurcation is situated at Re = 30 approximately, for Pr = 250 it is located at Re = 40. The second bifurcation suffers a more pronounced displacement regarding Reynolds number: for Pr = 1 it is located at Re = 60 but for Pr = 100 it is at Re = 80 and for Pr = 250 at Re = 100.

- Second, fixing the Reynolds number to 40 and varying the Prandtl number (see Figure 16b) we obtain a reduction of the length of the vortices, reaching a symmetrical solution for Pr = 250. However, for a smaller Prandtl, the solution is asymmetric. In this aspect, the effect is similar to the Weissenberg number influence: the increase of Pr gives a more *stable* solution. In terms of the heat convection forces in relation with the diffusivity, we can state that the flow pattern is more stable when the heat convection forces are significantly higher than the heat diffusion.

The temperature contours can be observed in Figure 17 for two different Prandtl numbers considering in both cases Re = 40, Br = 1 and We = 0.1. Two main comments can be done about the distribution of this field.

- The temperature contours are significantly different between the two cases. When the Prandtl numbers is small (Pr = 1), the thermal diffusivity is dominant compared to the convective term, and despite the inlet temperature being colder than on the walls, that fact does not affect the temperature distribution. In that case, the temperature is higher at the center of the duct, due to the effect of the viscous dissipation.

- However, in the case of Pr = 100, the convective term is now dominant, and therefore the cold inlet flow is distributed along the whole duct. For this reason, the gradient

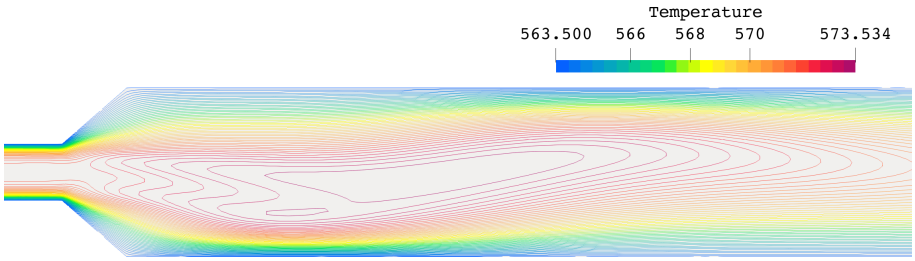


(a) Pr=1

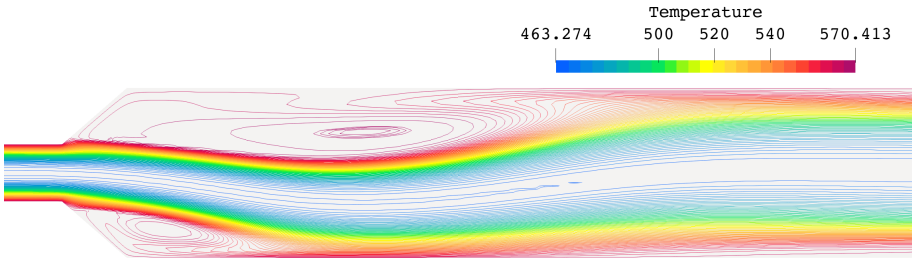


(b) Pr=100

Figure 17: 1:3 expansion. Distribution of temperature in the domain considering We = 0.1, Br = 1 and Re = 40 for two different Prandtl numbers: Pr = 1 (a) and Pr = 100 (b).

of the temperature is more pronounced in a channel cross-section (varying between 463.27 K to 570 K), and the maximum of temperatures induced by the internal work of the elastic fluid concentrates in the vortices. That effect is similar to the one reported in the case Pr = 1 and high Reynolds number (see Figure 11). In that case, the convective forces were also dominant but induced by a high advection velocity instead of a high heat capacity in comparison with the conductivity of the fluid flow.

### 5.2.5 Brinkman number study

Until this point, the effect of the Reynolds, Weissenberg, and Prandtl dimensionless numbers has been studied and characterized. In all the previous cases we have considered the Brinkman number as 1, as it was considered in the reference work [11]. By studying the influence for the four dimensionless numbers characteristics of the problem, we will see also how the Brinkman number affects the flow pattern. Note that this number compares the inertial power with the heat conduction, as explained previously. This dimensionless number can be understood as a global number that measures the coupling between flow and temperature. Therefore, following the same procedure as for the other dimensionless numbers studies, we display two different plots, represented in Figure 18.

- The first one (Figure 18a) represents the comparison of the vortex length for a range of Reynolds numbers and three Brinkman numbers: 1, 50, and 100. Note that for clarity, the same color is employed for representing the vortices of the same Brinkman number; nevertheless, different linestyles have been used to distinguish more clearly the length of each vortex and compare them. Let us remark that for computations where the Brinkman number is high, such as Br = 50 or Br = 100, new vortices emerge for low Reynolds number, also the size of the vortices is larger than in the case of Br = 1. Regarding the asymmetry, it occurs for a lower Reynolds number, (Re = 20) for Br = 50 and Br = 100, and also three vortices of different size appear simultaneously. For low Brinkman number, until Re = 66 the third vortex does

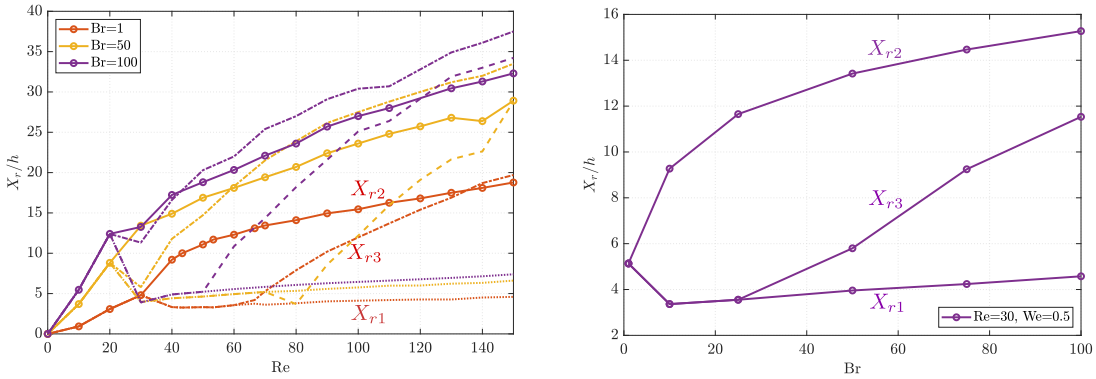


(a) (b)

Figure 18: 1:3 expansion. Effect of Brinkman number in vortex length, We = 0.1, Pr = 1. Length of vortices versus the Reynolds number (a), and length of vortices versus the Brinkman number for Re = 30 (b).

not appear, while for Br = 50, it occurs for approximately Re = 30. The fourth vortex emerges also for a low Reynolds number (Re = 45 in the case of Br = 100) in contrast with the low Brinkman number case, in which it is located at Re = 200 (see Figure 11).

- In Figure 18b, the lengths of the vortices are represented, fixing the Re = 40, We = 0.1 and Pr = 1. In this plot, the Brinkman effect can be observed with major clarity. For a decreasing Br the flow is stabilized until a stable symmetrical state is reached. In other words, the asymmetry is reduced and it is completely attenuated when the Brinkman number is 1. Otherwise, as the Brinkman number increases the flux becomes more *unstable*.

# 6 Conclusions

Throughout this work, the effect of the temperature coupling with viscoelastic fluid flows has been studied and analyzed. First of all, sub-grid scale VMS-stabilization methods have been proposed to obtain an accurate solution for high elastic flows. In this concern, two different formulations have been employed: both the standard and the log-conformation reformulation have been coupled with temperature. The log-conformation reformulation has been crucial for solving simulations with a high Weissenberg number, for which it is otherwise impossible to obtain converged solutions. Referring to the coupling, it is carried out in two different ways: on the one hand, viscoelastic properties are now temperature-dependent through defined functions. On the other, the energy equation has to consider the mechanical part of the elastic flow which is transformed into heat.

Regarding the numerical simulations, of the observed effects, two are the most remarkable: the first one is the increase of temperatures when the Weissenberg number increases, and the second one is a stress reduction in comparison with isothermal cases. However, in the particular case of the 1:3 expansion, also a thermal coupling effect to the flow pattern in the channel is found. In that case, we can observe that the asymmetric solution appears for lower Reynolds number in comparison with the isothermal case or a higher size of the vortices that emerge in both sides of the channel is observed. Moreover, the flow pattern is strongly influenced by the parameters that define the problem and for this reason, that influence has been explored varying the Prandtl number and the Brinkman number apart

from the Reynolds and Weissenberg numbers. As a general trend and for the models considered herein, the flow is more stable for low Re, high We, low Br and high Pr.

## Acknowledgements

Laura Moreno acknowledges the support received from the Spanish Government through a predoctoral FPI Grant. Ramon Codina acknowledges the support received from the ICREA Acadèmia Research Program of the Catalan Government. Joan Baiges acknowledges the support of the Spanish Government through the Ramón y Cajal grant RYC-2015-17367. This work is partially funded through the TOP-FSI project, Ref. RTI2018-098276-B-I00 of the Spanish Government.

## References

[1] H. Damanik, J. Hron, A. Ouazzi, and S. Turek. A monolithic FEM approach for the log-conformation reformulation (LCR) of viscoelastic flow problems. *Journal of Non-Newtonian Fluid Mechanics*, 165(19-20):1105–1113, 2010.

[2] G. W. M. Peters and F. P. T. Baaijens. Modelling of non-isothermal viscoelastic flows. *Journal of Non-Newtonian Fluid Mechanics*, 68(2-3):205–224, 1997.

[3] J. D. Ferry. *Viscoelastic properties of polymers*. John Wiley & Sons, 1980.

[4] M. L. Williams, R. F. Landel, and J. D. Ferry. The temperature dependence of relaxation mechanisms in amorphous polymers and other glass-forming liquids. *Journal of the American Chemical society*, 77(14):3701–3707, 1955.

[5] R. B. Bird, R. C. Armstrong, and O. Hassager. *Dynamics of polymeric liquids. Vol. 1: Fluid mechanics*. 1987.

[6] P. Lomellini. Viscosity-temperature relationships of a polycarbonate melt: Williams-Landel-Ferry versus Arrhenius behaviour. *Die Makromolekulare Chemie*, 193(1):69–79, 1992.

[7] F. T. Pinho and P. J. Oliveira. Analysis of forced convection in pipes and channels with the simplified Phan-Thien-Tanner fluid. *International journal of heat and mass transfer*, 43(13):2273–2287, 2000.

[8] P. M. Coelho, F. T. Pinho, and P. J. Oliveira. Fully developed forced convection of the Phan-Thien-Tanner fluid in ducts with a constant wall temperature. *International journal of heat and mass transfer*, 45(7):1413–1423, 2002.

[9] A. Jalali, M. A. Hulsen, M. Norouzi, and M. H. Kayhani. Numerical simulation of 3D viscoelastic developing flow and heat transfer in a rectangular duct with a nonlinear constitutive equation. *Korea-Australia Rheology Journal*, 25(2):95–105, 2013.

[10] F. Habla, A. Woitalka, S. Neuner, and O. Hinrichsen. Development of a methodology for numerical simulation of non-isothermal viscoelastic fluid flows with application to axisymmetric 4: 1 contraction flows. *Chemical engineering journal*, 207:772–784, 2012.

[11] A. Shahbani-Zahiri, M. M. Shahmardan, H. Hassanzadeh, and M. Norouzi. Effects of fluid inertia and elasticity and expansion angles on recirculation and thermal regions of viscoelastic flow in the symmetric planar gradual expansions. *Journal of the Brazilian Society of Mechanical Sciences and Engineering*, 40(10):480, 2018.

[12] K. Kunisch and X. Marduel. Optimal control of non-isothermal viscoelastic fluid flow. *Journal of Non-Newtonian Fluid Mechanics*, 88(3):261–301, 2000.

[13] C. L. Cox, H. Lee, and D. C. Szurley. Optimal control of non-isothermal viscous fluid flow. *Mathematical and computer modelling*, 50(7-8):1142–1153, 2009.

[14] M. M. A. Spanjaards, M. A. Hulsen, and P. D. Anderson. Computational analysis of the extrudate shape of three-dimensional viscoelastic, non-isothermal extrusion flows. *Journal of Non-Newtonian Fluid Mechanics*, 282:104310, 2020.

[15] N. Peres, A. M. Afonso, M. A. Alves, and F. T. Pinho. Heat transfer enhancement in laminar flow of viscoelastic fluids through a rectangular duct. In *Congreso de Métodos Numéricos en Ingeniería*, 2009.

[16] J. P. Hartnett and M. Kostic. Heat transfer to a viscoelastic fluid in laminar flow through a rectangular channel. *International journal of heat and mass transfer*, 28(6):1147–1155, 1985.

[17] M. A. Sheremet and I. Pop. Natural convection combined with thermal radiation in a square cavity filled with a viscoelastic fluid. *International Journal of Numerical Methods for Heat & Fluid Flow*, 2018.

[18] P.A. Christon, P.M. Gresho, and S.B. Sutton. Computational predictability of natural convection flow in enclosures. *Computational Fluid and Solid Mechanics*, pages 1465–1468, 2001.

[19] N. Phan-Thien and R. I. Tanner. A new constitutive equation derived from network theory. *Journal of Non-Newtonian Fluid Mechanics*, 2(4):353–365, 1977.

[20] N. Phan-Thien. A nonlinear network viscoelastic model. *Journal of Rheology*, 22(3):259–283, 1978.

[21] R. Fattal and R. Kupferman. Constitutive laws for the matrix-logarithm of the conformation tensor. *Journal of Non-Newtonian Fluid Mechanics*, 123(2-3):281–285, 2004.

[22] R. Fattal and R. Kupferman. Time-dependent simulation of viscoelastic flows at high weissenberg number using the log-conformation representation. *Journal of Non-Newtonian Fluid Mechanics*, 126(1):23–37, 2005.

[23] L. Moreno, R. Codina, J. Baiges, and E. Castillo. Logarithmic conformation reformulation in viscoelastic flow problems approximated by a VMS-type stabilized finite element formulation. *Computer Methods in Applied Mechanics and Engineering*, 354:706–731, 2019.

[24] D.-Y. Li, H. Zhang, J.-P. Cheng, X.-B. Li, F.-C. Li, S. Qian, and S. W. Joo. Numerical simulation of heat transfer enhancement by elastic turbulence in a curvy channel. *Microfluidics and Nanofluidics*, 21(2):25, 2017.

[25] T.J.R. Hughes, G. R. Feijóo, L. Mazzei, and J. Quincy. The variational multiscale method. A paradigm for computational mechanics. *Computer methods in applied mechanics and engineering*, 166(1-2):3–24, 1998.

[26] R. Codina. Stabilization of incompressibility and convection through orthogonal subscales in finite element methods. *Computer methods in applied mechanics and engineering*, 190(13-14):1579–1599, 2000.

[27] R. Codina. Stabilized finite element approximation of transient incompressible flows using orthogonal subscales. *Computer Methods in Applied Mechanics and Engineering*, 191(39-40):4295–4321, 2002.

[28] R. Codina. Analysis of a stabilized finite element approximation of the Oseen equations using orthogonal subscales. *Applied Numerical Mathematics*, 58:264 – 283, 2008.

[29] E. Castillo and R. Codina. Stabilized stress–velocity–pressure finite element formulations of the Navier–Stokes problem for fluids with non-linear viscosity. *Computer methods in applied mechanics and engineering*, 279:554–578, 2014.

[30] E. Castillo and R. Codina. Variational multi-scale stabilized formulations for the stationary three-field incompressible viscoelastic flow problem. *Computer Methods in Applied Mechanics and Engineering*, 279:579–605, 2014.

[31] P. C. Sousa, F. T. Pinho, and M. A. Alves. Purely-elastic flow instabilities and elastic turbulence in microfluidic cross-slot devices. *Soft matter*, 14(8):1344–1354, 2018.

[32] A. Groisman and V. Steinberg. Elastic turbulence in a polymer solution flow. *Nature*, 405(6782):53, 2000.

[33] C. M. White and M. G. Mungal. Mechanics and prediction of turbulent drag reduction with polymer additives. *Annu. Rev. Fluid Mech.*, 40:235–256, 2008.

[34] P. C. Sousa, P. M. Coelho, M. S. N. Oliveira, and M. A. Alves. Effect of the contraction ratio upon viscoelastic fluid flow in three-dimensional square–square contractions. *Chemical Engineering Science*, 66(5):998–1009, 2011.

[35] Y. Kwon. Numerical aspects in modeling high deborah number flow and elastic instability. *Journal of Computational Physics*, 265:128–144, 2014.

[36] H. Giesekus. A simple constitutive equation for polymer fluids based on the concept of deformation-dependent tensorial mobility. *Journal of Non-Newtonian Fluid Mechanics*, 11(1-2):69–109, 1982.

[37] Y. Mu, G. Zhao, X. Wu, and J. Zhai. Modeling and simulation of three-dimensional planar contraction flow of viscoelastic fluids with PTT, Giesekus and FENE-P constitutive models. *Applied Mathematics and Computation*, 218(17):8429–8443, 2012.

[38] J. M. Nóbrega, F. T. D. Pinho, P. J. Oliveira, and O. S. Carneiro. Accounting for temperature-dependent properties in viscoelastic duct flows. *International journal of heat and mass transfer*, 47(6-7):1141–1158, 2004.

[39] P. Wapperom and M. A. Hulsen. Thermodynamics of viscoelastic fluids: the temperature equation. *Journal of Rheology*, 42(5):999–1019, 1998.

[40] P. M. Coelho and F. T. Pinho. Fully-developed heat transfer in annuli with viscous dissipation. *International journal of heat and mass transfer*, 49(19-20):3349–3359, 2006.

[41] R. Codina, S. Badia, J. Baiges, and J. Principe. *Variational Multiscale Methods in Computational Fluid Dynamics,* in Encyclopedia of Computational Mechanics (eds E. Stein, R. Borst and T. J. R. Hughes), pages 1–28. John Wiley & Sons Ltd., 2017.

[42] R. Codina, E. Oñate, and M. Cervera. The intrinsic time for the streamline upwind/petrov-galerkin formulation using quadratic elements. *Computer Methods in Applied Mechanics and Engineering*, 94(2):239–262, 1992.

[43] L. Moreno, R. Codina, and J. Baiges. Solution of transient viscoelastic flow problems approximated by a term-by-term vms stabilized finite element formulation using time-dependent subgrid-scales. *Computer Methods in Applied Mechanics and Engineering*, 367:113074, 2020.

[44] E. Castillo, L. Moreno, J. Baiges, and R. Codina. Stabilised variational multi-scale finite element formulations for viscoelastic fluids. *Archives of Computational Methods in Engineering*, 28:1987–2019, 2021.

[45] H. P. W. Baaijens, G. W. M. Peters, F. P. T. Baaijens, and H.E.H. Meijer. Viscoelastic flow past a confined cylinder of a polyisobutylene solution. *Journal of Rheology*, 39(6):1243–1277, 1995.

[46] P. J. Oliveira. Asymmetric flows of viscoelastic fluids in symmetric planar expansion geometries. *Journal of non-newtonian fluid mechanics*, 114(1):33–63, 2003.

[47] R. M. Fearn, T. Mullin, and K. A. Cliffe. Nonlinear flow phenomena in a symmetric sudden expansion. *Journal of Fluid Mechanics*, 211:595–608, 1990.

[48] D. Drikakis. Bifurcation phenomena in incompressible sudden expansion flows. *Physics of Fluids*, 9(1):76–87, 1997.

[49] T. Hawa and Z. Rusak. The dynamics of a laminar flow in a symmetric channel with a sudden expansion. *Journal of Fluid Mechanics*, 436:283, 2001.

[50] G. N. Rocha, R. J. Poole, and P. J. Oliveira. Bifurcation phenomena in viscoelastic flows through a symmetric 1: 4 expansion. *Journal of non-newtonian fluid mechanics*, 141(1):1–17, 2007.

[51] S. Mishra and K. Jayaraman. Asymmetric flows in planar symmetric channels with large expansion ratio. *International journal for numerical methods in fluids*, 38(10):945–962, 2002.

[52] F. Durst, J. C. F. Pereira, and C. Tropea. The plane symmetric sudden-expansion flow at low reynolds numbers. *Journal of Fluid Mechanics*, 248:567–581, 1993.